



UNIVERSITY OF VICTORIA

## CENTRE FOR EARTH AND OCEAN RESEARCH (CEOR)

Flow Measurements in a Tidal Channel  
using an Acoustic Current Profiler

by:

Y. Lu and R.G. Lueck

CEOR Report: 96-2

March 1996

**Postal Address**

University of Victoria  
PO Box 1700  
Victoria, British Columbia  
Canada V8W 2Y2

Tel: (604) 721-8848

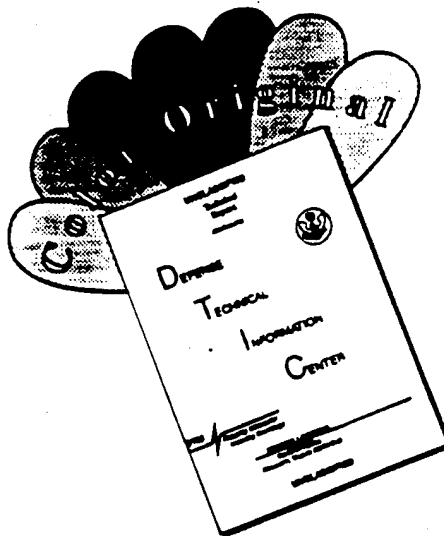
Fax: (604) 721-6200

DTIC QUALITY INSPECTED 1

**DISTRIBUTION STATEMENT 1**

Approved for public release;  
Distribution Unlimited

# DISCLAIMER NOTICE



THIS DOCUMENT IS BEST QUALITY AVAILABLE. THE COPY FURNISHED TO DTIC CONTAINED A SIGNIFICANT NUMBER OF COLOR PAGES WHICH DO NOT REPRODUCE LEGIBLY ON BLACK AND WHITE MICROFICHE.

Flow Measurements in a Tidal Channel  
using an Acoustic Current Profiler

by:

Y. Lu and R.G. Lueck

CEOR Report: 96-2

March 1996

DISTRIBUTION STATEMENT A

Approved for public release;  
Distribution Unlimited

19960422 023

Flow Measurement in a Tidal Channel  
Using  
an Acoustic Doppler Current Profiler

by

Youyu Lu and Rolf G. Lueck

School of Earth and Ocean Sciences,  
University of Victoria,  
Victoria, B.C.,  
Canada V8W 2Y2.

*February, 1996*

### **Abstract.**

An acoustic Doppler current profiler (ADCP) was applied to measure the three-dimensional flow field in a tidal channel along the coast of Vancouver Island, British Columbia. The ADCP was rigidly mounted to the bottom in the center of the channel, and rapidly sampled the velocity profiles along its inclined beams. The data were directly read by a computer on shore. This method of deployment allows for an explicit estimate of the uncertainty of mean velocity due to turbulence, and obtains the weak signal of vertical velocity. The mean flow vector is derived from the measured beam velocities under the assumption that the flow is statistically homogeneous in the horizontal plane over the distance separating the inclined beams of the ADCP. It is argued that sufficient averaging is required for flow measurements in a highly turbulent environment.

The depth-time variations of velocity and shear in this natural channel are more complex than is found in idealized one-dimensional channel flow, which seldom occurs in nature. The channel contains strong secondary circulation, intense up- and down-welling intervals, frequent shear reversals and a substantial amount of transverse velocity shear.

## 1. Introduction

Flow in shallow, coastal waters is complicated in its space-time variations. Good current measurements are essential for understanding coastal dynamics, developing and testing numerical models, and solving environmental problems. The most significant flow component is usually the tidal current, which is turbulent, and is influenced by the complex bottom topography and coastal geometry typically found in natural channels. For example, observations have shown that transverse circulation is generated by the flow curvature, and flow separation can occur near headlands (Geyer, 1993) or in the lee of islands (Wolanski et al., 1984). The transverse flow and flow separation may induce up/down-welling, by the mechanisms proposed by Garrett and Loucks (1976), and Wolanski et al. (1984).

Oceanic current are conventionally measured by deploying various types of current meters. A current meter measures the flow at a fixed position, hence an array of meters are needed to study the flow structure. The advent of acoustic Doppler current profilers (ADCP) provides an efficient way to measure velocity profiles. The spatial resolution and range in profiling are usually adequate to measure the flow and shear throughout a large portion of the water column in coastal seas. However, the velocity measured by a standard ADCP is the radial speed along each of its four beams which are inclined  $30^\circ$  to the centerline of the instrument. The true velocity vector is derived

from the measured velocities along beam pairs. The derivation assumes that the flow is homogeneous in horizontal plane over the distance separating the beams (e.g., Lohrmann et al, 1990). In a turbulent environment, this assumption may only hold statistically. Hence averaging is required, and only the time mean velocity vector can be obtained. From this point of view, an ADCP is not equivalent to an array of current meters equally spaced over the profiling range, as the latter does not involve the homogeneity requirement. Turbulence also introduces a statistical uncertainty in the mean velocity estimates, hence each mean ensemble must contain sufficient samples to reduce the uncertainty to an acceptable level. The vertical flow is usually weak, requiring that the ADCP is mounted rigidly so that this component is not influenced by the platform motions.

The results to be presented are based on data collected with an ADCP mounted rigidly to the bottom of Cordova Channel, British Columbia. This contribution describes the "mean" flow in the channel, i.e., those with time scales long compared to the turbulence. Section 2 describes the experiment setup. Section 3 provides the calculation algorithm. In section 4, we present a detailed data analysis, to determine the uncertainties in the mean velocity estimates from various sources, and to justify the averaging time chosen for the calculation of the mean. The observed depth-time variation of the flow and shear are presented in section 5. The deployment methods and the

channel flow dynamics are discussed in section 6. A summary is provided in section 7.

## **2. Experiment setup**

The measurements were taken in Cordova Channel in September 19-30, 1994, during a multi-investigator experiment. A broadband 600 KHz ADCP was located in the center of the channel where it is about 1 km wide and 30 m deep (figure 1). The coast line at the western side of the channel presents a headland (Cordova Spit), with shallow water in Saanichton Bay to the north (see the 20-m isobath). At the eastern boundary of the channel, James Island provides a small curvature, and both the northern and southern tips of the Island are within the tidal excursion distance from the site of ADCP. The water depth is fairly uniform along the axis of the channel.

The transducers on the ADCP were held 1.59 m above the bottom by a metal quadri-pod sitting on the seabed. The tilt sensors of the ADCP measured heading, pitch and roll angles with  $0.01^\circ$  resolution and the readings were steady throughout the experiment. Hence the instrument was rigidly mounted. Because the magnetic field was distorted by the metal stand, the compass readings were not correct, the true heading angle was determined to be  $150.3^\circ$  through a post-experimental calibration. A shore cable 800 m long connected the ADCP to the power supply and a computer in the shore station, and was used to send instructions and to communicate data.



A total length of 4.5 days of data were collected using the routine working mode (mode 4) of the ADCP which provides the maximum profiling range. The profiling range was limited to 27.6 meters above the bottom by the side lobes from the transducer reflected from the surface. The profiling range was broken up into uniform segments (called velocity bins) with 1 m spacing. The position of the center of the first velocity bin above the bottom was restricted by the height of the quadri-pod and a 1.5 m blanking distance after transmission. The centers of useful bins were 3.6-27.6 m above the bottom.

The velocity was recorded in beam coordinates with each beam nominally inclined by  $30^\circ$  from the vertical. The ADCP pinged at the fastest rate possible, about 0.75 second per ping or at a frequency of 1.3 Hz. The number of pings averaged by the ADCP into ensembles ranged from 2 to 4. The detailed data analysis presented in section 4 are based on the 4-ping averaged ensembles collected between day 23.9 to 25.

Throughout the experiment, winds were typically less than  $3 \text{ m s}^{-1}$  and only reached  $5 \text{ m s}^{-1}$  occasionally, hence the surface stress was negligible. A moored CTD observed a general warming trend of  $1^\circ\text{C}$  coupled with a decrease in salinity of 1.5 psu over the 9 days of the experiment, and also some moderate short-term variability. CTD profiles obtained by the IOS (Institute of Ocean Sciences, Patricia Bay, B.C.) group show that the strat-

ification in the channel changes with time, and the water below mid-depth (about 15 meters) is fairly homogeneous. Currents peak at about  $1 \text{ m s}^{-1}$ . During the experiment, the tide changed from spring to neap and the diurnal constituents became increasingly dominant.

### 3. Calculation algorithm

The velocity along a beam at any cell is the vector sum of the horizontal and vertical components at the position of that cell. The beam configuration is illustrated by figure 2, with  $\varphi_{1,2,3}$  representing the heading, pitch and roll angles respectively. Denote the velocity along the  $i$ -th beam as  $b_i$  ( $i=1$  to 4) and the velocity vector at the position of  $b_i$  as  $(u_i, v_i, w_i)$ . (There should be one more index denoting the order of bins, or depth cells. This index is dropped because we are considering only a single bin.) At first, we will not consider the heading angle  $\varphi_1$ , because it only involves rotation in the horizontal plane. Then for small pitch and roll angles and correct to the first order in  $\varphi_2$  and  $\varphi_3$ , one obtains (Lohrmann et al, 1990)

$$\begin{aligned}
 b_1 &= -u_1(\sin \theta + \varphi_3 \cos \theta) - w_1(\cos \theta - \varphi_3 \sin \theta) + v_1 \varphi_2 \cos \theta \\
 b_2 &= u_2(\sin \theta - \varphi_3 \cos \theta) - w_2(\cos \theta + \varphi_3 \sin \theta) + v_2 \varphi_2 \cos \theta \\
 b_3 &= -v_3(\sin \theta - \varphi_2 \cos \theta) - w_3(\cos \theta + \varphi_2 \sin \theta) - u_3 \varphi_3 \cos \theta \\
 b_4 &= v_4(\sin \theta + \varphi_2 \cos \theta) - w_4(\cos \theta - \varphi_2 \sin \theta) - u_4 \varphi_3 \cos \theta
 \end{aligned} \tag{1}$$

where  $\theta = 30^\circ$  is the beam inclination angle with respect to the centerline of the ADCP.

We define four quantities as

$$\begin{aligned}\hat{u} &= \frac{b_2 - b_1}{2 \sin \theta} - \varphi_3 \frac{b_1 + b_2}{2 \cos \theta} \\ \hat{v} &= \frac{b_4 - b_3}{2 \sin \theta} + \varphi_2 \frac{b_3 + b_4}{2 \cos \theta} \\ \hat{w} &= -\frac{b_1 + b_2 + b_3 + b_4}{4 \cos \theta} - \varphi_3 \frac{b_2 - b_1}{2 \sin \theta} + \varphi_2 \frac{b_4 - b_3}{2 \sin \theta} \\ \hat{e} &= -\frac{(b_1 + b_2) - (b_3 + b_4)}{4 \cos \theta}\end{aligned}\quad (2)$$

where  $(\hat{u}, \hat{v}, \hat{w})$  and  $\hat{e}$  are combinations of the measured beam velocities. When the ADCP operates in the “earth coordinates” mode, the transformation in (2) and a compass rotation is applied to the echo from every ping to produce the “velocity vector” and the “error velocity”. We operated in “beam coordinate” mode in which no transformation are applied and the beam velocities are returned directly. The relationship between  $(\hat{u}, \hat{v}, \hat{w}, \hat{e})$  and  $(u_i, v_i, w_i)$ , correct to the first order in  $\varphi_2$  and  $\varphi_3$ , can be derived to read

$$\begin{aligned}\hat{u} &= \frac{u_1 + u_2}{2} - \frac{w_2 - w_1}{2 \tan \theta} - \varphi_3 \frac{u_2 - u_1}{\sin 2\theta} + \varphi_2 \frac{v_2 - v_1}{2 \tan \theta} \\ \hat{v} &= \frac{v_3 + v_4}{2} - \frac{w_4 - w_3}{2 \tan \theta} + \varphi_2 \frac{v_4 - v_3}{\sin 2\theta} - \varphi_3 \frac{u_4 - u_3}{2 \tan \theta} \\ \hat{w} &= \frac{w_1 + w_2 + w_3 + w_4}{4} - \frac{(u_2 - u_1) + (v_4 - v_3)}{4} \tan \theta \\ &\quad + \varphi_3 \frac{(u_3 + u_4) - (u_1 + u_2)}{4} - \varphi_2 \frac{(v_3 + v_4) - (v_1 + v_2)}{4} \\ &\quad + \left( \varphi_3 \frac{w_2 - w_1}{2} - \varphi_2 \frac{w_4 - w_3}{2} \right) \frac{1 + \cos^2 \theta}{\sin 2\theta}\end{aligned}\quad (3)$$

$$\begin{aligned}\hat{e} = & \frac{(w_1 + w_2) - (w_3 + w_4)}{4} - \frac{(u_2 - u_1) - (v_4 - v_3)}{4} \tan \theta \\ & + \varphi_3 \frac{(u_1 + u_2) - (u_3 + u_4)}{4} - \varphi_2 \frac{(v_1 + v_2) - (v_3 + v_4)}{4} \\ & + \left( \varphi_3 \frac{w_2 - w_1}{4} + \varphi_2 \frac{w_4 - w_3}{4} \right) \tan \theta\end{aligned}$$

Clearly,  $(\hat{u}, \hat{v}, \hat{w})$  do not form a true velocity vector in general. For the special case of a velocity field that is instantaneously homogeneous in the horizontal plane over the distances separating the beams, (3) does give the true velocity vector on a ping-by-ping basis and  $\hat{e}$  is identically zero.

In a turbulent flow, however, the velocity fluctuations at the four beams are not instantaneously identical. Thus, the instantaneous horizontal and vertical components of the velocity cannot be measured with the ADCP. If the scale of variations of channel geometry are very large compared to the separation of the beams, then the statistical properties of the flow can be assumed to be horizontally homogeneous. In particular, we will assume that the mean components (horizontal and vertical) are horizontally homogeneous over the spatial domain of the beams and that the fluctuations average to zero. Thus, we decompose the velocity components  $(u_i, v_i, w_i)$  at the four beams into a mean field  $(\bar{u}, \bar{v}, \bar{w})$ , which is the same for all the four beams, and the turbulent fluctuations  $(u'_i, v'_i, w'_i)$ , which all average to zero but may be different at the four beams. Then, by averaging out the turbulent fluctu-

ations, (3) becomes

$$\begin{aligned}\overline{\hat{u}} &= \bar{u} \\ \overline{\hat{v}} &= \bar{v} \\ \overline{\hat{w}} &= \bar{w} \\ \overline{\hat{e}} &= \bar{e} = 0\end{aligned}\tag{4}$$

Hence the mean velocity vector  $(\bar{u}, \bar{v}, \bar{w})$  can be obtained by sufficient averaging under the assumption of statistical homogeneity in the horizontal plane. The amount of averaging required to give satisfactory estimates of the mean components is difficult to predict *a priori*. The amount required will certainly depend upon the distribution of eddy scales and the energy of the eddies. For example, if all eddies have scales large compared to the beam separations, then the field is instantaneously homogeneous and the statistical uncertainty of the estimates is determined solely by the probability distribution of the fluctuations and the degrees of freedom. For such eddies, the vertical velocity must be small compared to the horizontal components owing to its bottom boundary condition. The most intense vertical velocities will come from eddies with scales comparable to the distance from the bottom which is almost the same as the distance separating beam pairs. The averaging will have to span many such eddies which is realized with an averaging time  $\tau \gg L/U$  where  $L$  is the beam separation, which ranges from 2.3 to 31 m, and  $U$  is the mean speed. Averaging over a fixed length scale is not

very practical. We chose an averaging time of 20 minutes. The least amount of spatial averaging occurs for weak flows and amounts to only 120 m in a current of  $0.1 \text{ m s}^{-1}$ . For typical flows of  $1 \text{ m s}^{-1}$ , the averaging scale is 1200 m and the ratio of averaging scale to beam separation is 39 and 520 for the top and bottom of the profiles, respectively.

The only explicit test of the averaging is provided by the redundant estimates of vertical velocity from the two beam pairs. The error velocity  $\hat{e}$  in (2) and (3) is half the difference between these two estimates of the vertical velocity. The averaging is insufficient or the assumption of horizontal homogeneity is invalid if the error velocity is not small compared to the estimated vertical velocity. The error velocity is not always small compared to the vertical velocity in the upper half of the profiling range during weak flows.

For a rigidly mounted ADCP, the values of tilt angles  $\varphi_i (i = 1, 2, 3)$  are constant and the beam velocities can be averaged first to estimate the mean velocity components from (2), that is,

$$\begin{aligned}\bar{u} &= \frac{\bar{b}_2 - \bar{b}_1}{2 \sin \theta} - \varphi_3 \frac{\bar{b}_1 + \bar{b}_2}{2 \cos \theta} \\ \bar{v} &= \frac{\bar{b}_4 - \bar{b}_3}{2 \sin \theta} + \varphi_2 \frac{\bar{b}_3 + \bar{b}_4}{2 \cos \theta} \\ \bar{w} &= -\frac{\bar{b}_1 + \bar{b}_2 + \bar{b}_3 + \bar{b}_4}{4 \cos \theta} - \varphi_3 \frac{\bar{b}_2 - \bar{b}_1}{2 \sin \theta} + \varphi_2 \frac{\bar{b}_4 - \bar{b}_3}{2 \sin \theta} \\ \bar{e} &= -\frac{(\bar{b}_1 + \bar{b}_2) - (\bar{b}_3 + \bar{b}_4)}{4 \cos \theta}\end{aligned}\tag{5}$$

Because the velocity along the beams,  $b_i (i = 1 \text{ to } 4)$ , can be measured instan-

taneously, the uncertainty of their means can be evaluated from the standard deviation of the along-beam fluctuations  $b'_i$ . The statistics of the along-beam means can then be used to estimate the confidence interval for the mean flow vector  $(\bar{u}, \bar{v}, \bar{w})$ .

Would a moored ADCP give results comparable to a rigidly mounted unit? A moored instrument would have fluctuating tilt angles but a close examination of (3) indicates that this is unlikely to have significant effects. All products involving mean tilt angles and mean velocities would vanish just like they do for a rigidly mounted instrument. Products involving fluctuating tilts and mean velocity, and vice versa, vanish by assumption. Only a potential correlation between fluctuating tilt angles and velocity differentiates the two mounting configurations. For example, the term  $\overline{\varphi'_3(u'_2 - u'_1)}$  from the first line in (3) may be non-zero. The location of the velocity fluctuations is removed from the position of the instrument and only fluctuations with very large scales are likely to be coherent at the two positions. The coherence would be equally good at the position of the two velocity measurements which makes the correlation small. Similarly if  $u'_2$  and  $u'_1$  are not coherent then neither is likely to be coherent with tilt fluctuations which, again, makes the correlation of tilt and velocity small. However, the tilting of a moored instrument is unlikely to be centered around its transducers and translational movement of the transducers is inevitable. The translational

motion, which is not monitored by the instrument, will add vectorially to the beam velocities and, thus, the measured beam velocities will be contaminated. Translational motion will be highly correlated with fluctuations of tilt. The vertical velocity, which is small compare to the horizontal components, is unlikely to be well estimated by an instrument buffeted by turbulent fluctuations. Without reliable estimates of vertical velocity, the error velocity is also unreliable. Thus, it may be impossible to test either the assumption of horizontal homogeneity or the adequacy of the averaging for a moored ADCP in a highly turbulent flow.

#### 4. Data analysis

##### *a. Correction of tilting angles*

Inaccuracy in the pitch and roll angles measured by the tilt sensors introduces errors in the derivation of velocity vector from beam velocities. This affects the calculation of the vertical velocity most because it is weak compared to the horizontal components and is easily contaminated. The measured values of  $\varphi_2$  and  $\varphi_3$  are  $0.00^\circ$  and  $-3.00^\circ$  respectively throughout the experiment. Using these two values, however, the calculated vertical velocity at mid-depth includes a tidally varying signal (figure 3, thinner lines). This signal is not the true vertical flow, but rather the contamination by the horizontal velocity. By choosing combinations of different values of  $\varphi_2$  and  $\varphi_3$ , we found that this tidal signal can be minimized by changing the roll angle from  $-3.0^\circ$  to  $-2.0^\circ$



(thicker lines, figure 3). Hence the values of  $\varphi_{1,2,3}$  used in the calculation are  $(150.3^\circ, 0.0^\circ, -2.0^\circ)$ .

*b. Measurement uncertainties*

The measured beam velocity contains an uncertainty due to the Doppler noise. To determine the level of this noise, an *in situ* test was conducted by mounting the ADCP, looking downward, on a boat drifting in the almost slack water of Saanich Inlet. The signal associated with the motion of the boat was removed by subtracting a second-order polynomial fit from each along-beam velocity profile. The remaining signals are taken as Doppler noise. Figure 4 shows that the standard deviation of the beam velocity noise is  $0.01\text{--}0.015 \text{ m s}^{-1}$  up to a profiling range of 40 m, for 4-ping averaged ensembles with 1 m bin size. The consecutive ensembles are uncorrelated. Hence by averaging  $N$  ensembles together the noise standard deviation is reduced by a factor of  $N^{1/2}$ . For 20-minute averages, the uncertainty in beam velocity is  $5\text{--}7 \times 10^{-4} \text{ m s}^{-1}$ .

For the mean velocity estimates, turbulent fluctuations introduce another source of uncertainty. Figure 5 shows a sample of one-day long, 4-ping averaged beam velocity at mid-depth from beam No.1, the beam oriented in the downstream direction during the ebb. The flow is southward during the ebb and northward during the flood. A low-pass 4-th order butterworth filter, with zero-lag and a cut-off period of 20 minutes, was applied to separate

the low- from high-frequency variations. The intensity of fluctuations, as seen from the high-frequency residue, is not stationary throughout the tidal cycle. Figure 6 shows the standard deviation of beam velocity fluctuations, calculated over 20-minute intervals, for beams No.1 and No.3 at two depths (beam No.3 was oriented approximately in the cross-channel direction). The time-variation in the standard deviation is obvious. The rms velocity fluctuation is about  $0.05 \text{ m s}^{-1}$  at peak flow, reaches up to  $0.1 \text{ m s}^{-1}$  during the flow turning at day 24.05, and decreases to  $0.015 \text{ m s}^{-1}$  at the weak flood between day 24.6 and 24.8. Hence turbulence dominates the high-frequency fluctuations shown in figure 5, and is only comparable to the Doppler noise during the weak flood.

Most statistical analysis requires data that is stationary, or homogeneous, in the time domain of interests. To examine the stationarity over short time intervals, we plot two sections of the 20-minute long time series of the velocity fluctuations, one taken during the strong ebb starting at day 23.91 (figure 7), and the other taken during the flow turning starting at day 24.03 (figure 8). The high-pass velocity fluctuations plotted are along beams No.1 and No.3, at the heights of 3.6 m and 15.6 m respectively. The turbulent fluctuations can be viewed as stationary for the 20-minute interval during the strong ebb, but the fluctuations during flow turning are not stationary. A strong event lasting about 100 seconds, with changes in beam velocity exceeding  $0.4 \text{ m s}^{-1}$ ,

happened during flow turning. In fact, the large values of the beam velocity standard deviation during this time interval (figure 6) is attributable to this single event.

Figure 9 shows the auto-correlation functions (acf) against the time lag  $\tau$ , for the beam velocity fluctuations shown in figure 7. The uncertainty level of the acf estimates. These correlation functions are not like that for a white noise. A de-correlation time scale is defined as the time lag when an acf is reduced to the upper band of its uncertainty level, which is estimated to be 0.1. For this 20-minute-long data, the de-correlation time is about 35 s for the velocity along beam No. 1 at 3.6 m above the bottom (figure 9(c)) and is about 15 s for the other three acf's. These de-correlation time scales correspond to the scales of the dominant turbulent eddies. Following Taylor's hypothesis and using the 20-minute mean horizontal velocity, the de-correlation time scales found above imply that these eddies have (horizontal) spatial scales ranging between 15 and 30 m during this strong flow interval. In comparison, the acf's of the velocity fluctuations for the 20-minute interval starting at day 24.6 during the weak flood look more like that for a white noise (figure 10). This may simply due to the Doppler noise which is comparable to turbulent intensities during this time interval.

Choosing 15 sec as a typical de-correlation time gives 80 independent samples in a 20-minute interval. The standard deviation of the rapidly sampled

beam velocity is of  $O(0.05)$   $\text{m s}^{-1}$  typically during the strong flow (figure 6). For 20-minute averaging, the rms velocity fluctuation is reduced to 0.0055  $\text{m s}^{-1}$ , 8-11 times larger than that due to Doppler noise. The standard deviation of the 20-minute mean beam velocity is 0.0017  $\text{m s}^{-1}$  during the weak flood between day 24.6 and 24.8, and, still dominates that of the Doppler noise.

Including terms representing the uncertainty in the mean beam velocity in equation (5), one can deduce that the standard deviations of the horizontal and vertical velocity components are  $\sqrt{2}$  times larger and  $\sqrt{3}$  times smaller respectively than that of the beam velocity. Thus the uncertainty due to turbulence in the 20-minute mean velocities is about 0.008  $\text{m s}^{-1}$  for  $(\bar{u}, \bar{v})$  and 0.003  $\text{m s}^{-1}$  for  $\bar{w}$  typically at strong flow, and the level of uncertainty during the weak flood between day 24.6 and 24.8 is three times smaller.

The non-zero acf's at considerably long lags, as shown in figures 9 and 10, reflect the eddies with sizes larger than those of the dominant ones. For the time interval during the flow turning, shown in figure 8, the distinct event lasting 100 sec dominates the eddies with shorter time scales. Figure 5 shows that a smoothing of beam velocity at 20-minute cutoff period not only keeps the tidal signal, but some eddy fluctuations with periods longer than 20 minutes as well. To smooth out the fluctuations due to these eddies requires averaging over scales larger than the size of these eddies. However, choosing a longer averaging period may conflict with the requirement to keep

the variations at tidal frequencies.

*c. The choice of averaging period*

In dealing with unstationary tidal flow, the choice of an appropriate averaging time is usually hard to make. This is because the "spectral gap" separating turbulence from the tidal fluctuations is "something which *a priori* may not be known to exist or physically need to exist", as noted by Gross and Nowell (1983). A compromise is always needed between choosing a sufficiently long averaging time to reduce the uncertainties by turbulent eddies and choosing a shorter one to keep the tidal variations. For measurement using the ADCP, there is another constraint, i.e., the assumption of statistical homogeneity may also require sufficient averaging. The 20-minute averaging period chosen in this analysis reduces the rms velocity fluctuations due to the Doppler noise and turbulence to considerably low levels, compared to the mean velocity magnitude. The change of the tidal flow during the 20-minute intervals is obtained in the next section by taking a harmonic analysis for all the data. As was discussed in section 3, 20-minute averaging corresponds to averaging over spatial scales much larger than the beam separating distance during strong flow. Choosing a shorter averaging period is still acceptable at peak flow, but would be too short when the flow is weak. Whether or not choosing a shorter averaging time changes the estimate of the bottom stress from the log-layer fitting is addressed in the companion paper by Lueck and Lu (1996).

## 5. Results

### *a. Tidal and non-tidal variations*

The 4.5-day long data collected using mode 4 spanned 8 days during the experiment. Figure 11 shows the 20-minute mean horizontal flow at mid-depth and the harmonic fit composed of four major tidal constituents ( $M_2$ ,  $S_2$ ,  $K_1$  and  $O_1$ ) and the zero-frequency residue. The flow was rotated into two components along and transverse to the direction pointing  $345^\circ$  from north, which is approximately along the channel axis. The harmonic fit explains 95% of the variance in the observed flow at mid-depth and 91% at 4.6 m above the bottom. The record length of the data is not long enough to obtain accurate harmonic constants for all the constituents included. The point to make here is that the major signals in the observed channel flow are tidal. The change of flow by the tidal variations over the averaging time intervals chosen, here being 20-minutes, reaches up to  $0.15 \text{ m s}^{-1}$  at mid-depth during weak flow when the acceleration/deceleration rates are largest. Hence the change of flow due to tidal variation is much larger than the uncertainties due to Doppler noise and turbulence.

The difference between the data and the harmonic fit, is also shown in figure 11. Combining this difference with the zero-frequency residue, obtained from the harmonic fitting, gives the non-tidal variations of the channel flow. The non-tidal variations can be attributed to the large-scale eddies not be-

Table 1: The cross- and along-channel components of the zero-frequency residual flow and the mean magnitude of the difference between the observed flow and the harmonic fit, in  $[m s^{-1}]$ . The error bars of the mean magnitude are the 95% confidence intervals obtained using a bootstrap method.

$z$ [m]	residue	mean magnitude of the “difference”		
		all	ebb	flood
15.6	(0.03,-0.17)	$0.090 \pm 0.007$	$0.097 \pm 0.010$	$0.078 \pm 0.010$
4.6	(-0.02,-0.14)	$0.143 \pm 0.009$	$0.161 \pm 0.013$	$0.116 \pm 0.011$

ing smoothed out by the 20-minute averaging, and the secondary circulation generated mainly by the curvature forcing of the headland. Table 1 lists the cross- and along-channel components of the zero-frequency residue and the mean magnitude of the difference between the observed flow and the harmonic fit at two heights, i.e., at mid-depth and 4.6 m above the seabed respectively. The magnitude of the “difference” is also calculated for the ebb and the flood phases separately. The error bars associated with the mean magnitude is the 95% confidence interval calculated using a bootstrap method (Efron and Tibshirani, 1993). The zero-frequency residual flow is southward. The departure of the flow from the harmonic fit intensifies near the bottom, and is larger during the ebb than during the flood. The departures of the velocity from the tidal fit are attributed, in the following sections, to asymmetry of the secondary circulation with respect to the tide, and to large-scale eddies generated by flow separation from the headland during the ebb.

*b. Asymmetry between the flood and the ebb*

The 20-min mean velocity profiles of  $(\bar{u}(z), \bar{v}(z))$  are averaged over the profiling range, and referred to as the “depth-mean” flow, hereafter. The 4.5-day long data of the depth-mean flow magnitude and direction are plotted in a polar coordinate diagram (figure 12). The direction of the ebb is approximately  $160^\circ$  and the flood is approximately  $350^\circ$ , i.e., the two directions differ by only  $170^\circ$ . The ebb is stronger than the flood, consistent with the net southward flow obtained from the harmonic fitting. The current direction also changes vertically (figure 13). The direction difference between bottom and top layers is about  $15^\circ$  typically, both for flood and ebb. The veering with height during the flood is in the same direction as for a bottom Ekman layer, but the backing during the ebb is in the opposite sense. The vertical rotation of the shear (also shown in figure 13) is about  $90^\circ$ , much larger than for the flow. Comparing the direction of the shear and the flow at 3.6 m above the seabed, one can see that both are quite close during the flood, whereas the shear is about  $30^\circ$  counter-clockwise from the flow during the ebb (top panel, figure 13). The strong asymmetry in the direction of shear towards bottom, and the offset of shear direction from the current, are also illustrated by the polar coordinate diagrams of the 4.5-day long data (figure 14). The significant transverse shear during the ebb corresponds to a transverse bottom stress directed offshore from the headland (figure 1).



*c. Velocity and shear profiles*

The direction of the depth-mean flow is not constant. Defining the streamwise direction,  $s$ , as directed downstream of the depth-mean flow during the flood, and the transverse direction  $n$  being normal and to the right of  $s$ , we obtain an instantaneous orthogonal curvilinear system. Each 20-minute mean velocity profile  $(\bar{u}(z), \bar{v}(z))$  is rotated to components  $(u_s(z), u_n(z))$  along the  $s$  and  $n$  axes. The streamwise and transverse velocity shear,  $(\partial u_s / \partial z, \partial u_n / \partial z)$ , are calculated from the  $(u_s(z), u_n(z))$  profiles by applying a first difference for the top and bottom bins and a center difference for the middle bins. The uncertainty due to turbulence in the mean shear estimate is hence  $0.008 \text{ s}^{-1}$ .

Figure 15 shows the depth-time sections of one-day long streamwise and transverse flow  $(u_s, u_n)$  and shear  $(\partial u_s / \partial z, \partial u_n / \partial z)$ , as well as vertical velocity  $\bar{w}$ . Plots of time series and profiles of these quantities are provided (figures 16 to 19), to assist the interpretation of the color image. The streamwise flow (top panels in figures 15, 16) shows a strong tidal signal, with the flow in the lower layer diminished by the bottom drag. The non-tidal variations can be strong enough to distort the tidal variations. For example, the strong ebb between day 24.3 and 24.6 has two peaks and with weaker flow in between. The transverse flow is stronger in the near surface and near bottom layers, and weakest at mid-depth (second panels in figures 15, 16), Its magnitude reaches  $O(0.15 \text{ m s}^{-1})$  at the lowest bin during the ebb, and is

about  $O(0.05 \text{ m s}^{-1})$  in both the upper and the lower layers during the flood. The transverse flow is usually directed to the headland in the lower layer, and in the opposite direction in the upper layer, with exceptions during flow turning and the weak flood between days 24.6 and 24.8. Also during the ebb near day 23.9 and between days 24.85 and 25, the transverse flow shows a three-layer structure. Consecutive evolution (spaced by 40 minutes) of velocity profiles are illustrated in figure 17. The maximum speeds of streamwise flow are frequently found at heights below the upper most bin. The upper layer apparently leads the lower layer in the decelerating stage, whereas it lags during the accelerating stage. The transverse velocity profiles generally show a linear variation in magnitude with height in the lower layer, and more complex variations in the upper layer (figure 17).

Both the streamwise and the transverse shear are bottom-enhanced (two lower panels in figure 15; figures 18 and 19). The streamwise shear reaches a magnitude of  $O(0.05 \text{ s}^{-1})$  in the lower layer, and contains a strong tidal signal. The transverse shear reaches about half the magnitude of the streamwise shear near the bottom during the ebb, and is small during the flood. The streamwise shear frequently reverses sign near mid-depth, in accordance with the maximum flow speed below the surface (figure 17, top panel). The shear reversals may be due to the inertia of the oscillatory flow (this effect on near-bed velocity profile was discussed by Soulsby and Dyer, 1981). However, the

apparent preference of shear reversals occurring during the ebb suggests that they could result from the entrainment of shallow water from Saanichton Bay, which would slow down the water above mid-depth in the channel. Shear reversals are also found in the transverse direction during the ebb, and reflect the occurrence of a three-layer structure in the transverse flow.

*d. Vertical velocity*

The middle panel of figure 15 shows the 20-minute mean vertical velocity. Several significant up- and down-welling intervals can be identified, some happen during flow turning and some during strong currents. These intensified vertical flow intervals generally occur over the entire profiling range, although the maximum velocity is at mid-depth, reaching  $O(0.05 \text{ m s}^{-1})$  at times. Figure 20 compares the vertical velocity and the corresponding "error" velocity at three levels. The sign of the "error" velocity is kept the same as that of the vertical velocity, to facilitate the comparison of these two quantities. The magnitude of the "error" velocity is generally smaller than that of the vertical velocity at the lowest level. This indicates that for 20-minute averaging, the estimated mean velocity is homogeneous over the spread of the beams at the lower levels where the distance separating the beams is small. The magnitude of the "error" velocity increases with the increasing height. At the first peak of the vertical flow after day 24, which corresponds to the event shown in figure 8, the "error" velocity is large and

comparable with the vertical velocity at 15.6 and 27.6 m above the bottom. Other events at 15.6 m height have relatively small error velocities but the error velocity is frequently large at 27.6 m above the bottom. This means that 20-minute averaging is not sufficient to give satisfactory estimates of the mean flow at the upper levels where the beam spreading is large. Note an  $O(0.05 \text{ m s}^{-1})$  vertical flow lasting 20 minutes is enough to bring the bottom water to the surface and vice versa.

## 6. Discussions

### *a. ADCP deployment techniques*

Various techniques to deploy the ADCP were reported among the increasing applications of this instrument to oceanic measurements. For example, ADCP can be mounted on moving ships, looking downward, to take transects in a study area (e.g., Candela et al, 1992; Geyer, 1993; Gargett, 1994), mounted in a buoy (e.g., Schott and Johns, 1987; Johns, 1988; van Haren et al, 1994), in a trawl-resistance package (Tang and Belliveau, 1994), or mounted rigidly to the bottom (Lohrmann et al, 1990; and this work). The data recorded can be the beam velocities or the velocity vectors transformed by the internal processors. Ensemble averaging can be performed before recording. For self-contained deployment, the battery capacity and the memory space constrain the experiment duration, the length of the averaging interval, and the number of pings that can be averaged into an en-

semble. The direct-reading deployments as adopted in this study are free from these constraints, but there are still choices to be made in setting the profiling parameters. For either self-contained or direct-reading deployments, the profiling parameters set should ensure that the recorded data can derive meaningful results.

The derivation of velocity vectors from the beam velocities is based on the assumption that the flow field is homogeneous over the horizontal distance separating the beams. In a turbulent flow field, the homogeneity holds only statistically. Hence even though the beam velocities can be sampled at rapid rates, only the time averaged velocity vectors can be derived. For rigidly mounted deployment, averaging the beam velocity to derive the mean velocity vector gives the same results as averaging the individually transformed "velocity vector". For non-rigid mounting deployment, however, the transformation must be done from ping to ping as the orientation of the beams changes with time hence averaging the beam velocity is meaningless. The vertical flow is usually weak and is easily contaminated by small errors in the tilt angles, and the motions of a platform to which the ADCP is mounted. For a rigid mount without platform motions, a systematic bias in the measurement of tilt angle can be corrected through minimizing the mean vertical flow signal by changing the values of tilt angles. The vertical velocity is difficult to obtain for non-rigid deployments as the motions of the unstable

platforms such as ships or buoys are usually not easily determined. Thus, it may not be possible to test the homogeneity of the mean flow estimates by comparing the error velocity against the vertical velocity. The measurement of vertical flow using a modified ADCP with a true vertical beam (Gargett, 1994) also requires a sufficiently stable platform.

*b. Channel flow dynamics*

The measurement revealed a complicated picture of tidal flow in a natural channel. The curvature of the side boundaries of the channel, seen in figure 1, contributes to this complexity. Taking account of flow curvature, the momentum balance in the transverse flow direction,  $n$ , is

$$\frac{\partial u_n}{\partial t} + u_s \frac{\partial u_n}{\partial s} - \frac{u_s^2}{R} - f u_s = -g \frac{\partial \eta}{\partial n} + \frac{\partial}{\partial z}(-\overline{u'_n w'}) \quad (6)$$

where  $\eta$  is the free-surface elevation,  $g$  the acceleration due to gravity,  $f$  the Coriolis parameter, and  $R$  is the local radius of streamline curvature (for depth-mean flow). The effect due to stratification has been neglected. The other approximations made in writing (6) can mostly be justified by assuming  $O(u_n) < O(u_s)$  (see Kalkwijk and Booij, 1986). The second term in (6), representing the advection by the streamwise flow, was not measured. The relative importance of the curvature effect to Coriolis force can be quantified by a Rossby number  $R_o = u_s/(fR)$ . For  $f \sim 10^{-4} \text{ s}^{-1}$  and  $u_s \sim 1 \text{ m s}^{-1}$ ,  $R = 2, 10 \text{ km}$  gives  $R_o \sim 5$  and 1 respectively. During the ebb,  $u_n$  generated

by flow curvature is in the direction of the observed secondary circulation, and it is opposite to the contribution by Coriolis force. The secondary circulation generated by Coriolis force and curvature effect are along the same direction during the flood, and consistent with the observed circulation. The stronger transverse circulation observed during the ebb suggests that the streamlines have sharper curvature during this phase of the tide than during the flood.

The radius of streamline curvature is not known because the measurements were taken at a fixed site. However, a tentative guess can be made using the formulae derived by Kalkwijk and Booij (1986). Assuming that the log-layer in the streamwise direction extends to the surface, they got

$$u_{nc} = -\text{sign}(\bar{u}_s) \frac{fh}{\kappa^2} f_c\left(\frac{z}{h}, \alpha\right) \quad (7)$$

$$u_{nb} = 2 \frac{|\bar{u}_s|h}{\kappa^2 R} f_b\left(\frac{z}{h}, \alpha\right) \quad (8)$$

where  $u_{nc}$  denotes the contribution from Coriolis forcing and  $u_{nb}$  from the effect of curvature (bending);  $\bar{u}_s$  is the depth-mean of  $u_s$ ; and  $\alpha = C_D^{1/2}/\kappa$ . The two profile functions,  $f_c$  and  $f_b$ , are nearly linear functions of  $z$  except very close to bottom (their figure 2). Using our estimates of  $C_D \approx 4 \times 10^{-3}$  from fitting log-layers to the streamwise velocity profiles (Lueck and Lu, 1996) gives  $\alpha \approx 0.15$ , the magnitude of  $f_c$  and  $f_b$  in both the near-surface and bottom layers are  $O(0.5)$ . In Cordova Channel  $h \approx 30$  m and  $f \approx 10^{-4}$  s<sup>-1</sup>, for  $\bar{u}_s \approx 1$  m s<sup>-1</sup> we have  $u_{nc} \approx 0.01$  m s<sup>-1</sup>. Hence the Coriolis force does not dominate during either the flood or the ebb. Using the observed

secondary circulation during the flood and the ebb,  $u_{nb} \approx 0.05, 0.15 \text{ m s}^{-1}$  correspond to  $R \approx 4, 1.5 \text{ km}$  respectively. This implies that the streamline curvature may have a radius as small as 1.5 km during the ebb and more than 4 km during the flood. These scales are not inconsistent with the geometric and topographic features of Cordova Channel. During the ebb, the flow from the Saanichton Bay experiences a sharper curvature when turning around the headland. The channel is fairly straight to the south of the experiment site, hence during the flood, the flow aligns with the axis of the Channel and can over shoot the headland which produces a smaller curvature.

Geyer and Signell (1991), also Geyer (1993), observed flow separation for tidal flow passing a headland. The generation of horizontal eddies by tidal flow was also observed by Wolanski et al (1984) in the lee of an island. The sharp curvature experienced by the flow during the ebb in Cordova Channel may also favor the separation of flow, as suggested by visual observations in the Channel (Eric D'Asaro, personal communication, 1995).

## 7. Summary

In this study, a broadband ADCP was rigidly mounted to the bottom of Cordova Channel and the data were directly read by a computer on the shore. The rapid sampling of beam velocity profiles allows for an explicit estimate of the level of the uncertainty due to turbulence in the calculated mean velocity. It is argued that for flow measurement in highly turbulent



environment, averaging over sufficient large scales is required in accordance with the assumption of the flow being statistically homogeneous over the distance separating the beams of the ADCP. The 20-minute averaging period chosen in this analysis corresponds to averaging over scales large compared to the beam spreading, and also reduces the uncertainties in the mean flow and shear estimates caused by the Doppler noise and the dominant turbulent eddies. The stable platform provided by the rigid mounting enables removing the bias in the vertical velocity due to a systematic error in the measurement of tilt angles.

The depth-time variations of flow and shear observed in Cordova Channel are complicated. A harmonic analysis including the major tidal constituents explains more than 90% of the variance in the 20-minute mean velocities, indicating that the flow in the Channel is mainly tidal. Separating the horizontal flow into streamwise and transverse components, substantial transverse flow and velocity shear were observed, showing a strong influence of flow curvature provided by the headland at one side of the channel. The curvature effect dominates the Coriolis forcing in driving the transverse circulation. The streamwise shear is bottom-enhanced. The shear frequently reverses sign at mid-depth during the ebb, and this is attributed to the entrainment of the water from a shallow bay to the north of the channel. Intensified up- and down-welling events with magnitude reaching  $0.05 \text{ m s}^{-1}$  at mid-depth, are

observed. These large values of vertical velocity are validated by comparing them with the corresponding "error" velocities.

*Acknowledgment.* This work was supported by the Office of Naval Research under Grant N00014-93-1-0362.

## References

- Candela, J., R.C. Beardsley, and R. Limeburger, 1992. Separation of tidal and subtidal currents in ship-mounted Acoustic Doppler Current Profiler observations. *J. Geophys. Res.*, **97**, 769-788.
- Efron, B., and R. J. Tibshirani, 1993. *An Introduction to the Bootstrap*. Chapman & Hall, New York-London, pp436.
- Gargett, A.E., 1994. Observing turbulence with a modified acoustic Doppler current profile. *J. Atmos. Oceanic. Technol.*, **11**, 1592-1610.
- Garrett, C.J.R., and R.H. Loucks, 1976. Up-welling along the Yarmouth shore of Nova Scotia. *J. Fish. Res. Board of Can.*, **33**, 116-117.
- Geyer, W. R., 1993. Three-dimensional tidal flow around headlands. *J. Geophys. Res.*, **98**, 955-966.
- Geyer, W. R., and R. Signell, 1991. Measurements and modeling of the spatial structure of nonlinear tidal flow around a headland. In *Tidal Hydrodynamics*, Parker, B. B. (Ed.), John Wiley and Sons, 883pp.
- Gross, T.F., and A. R. M. Nowell, 1983. Mean flow and turbulence scaling in a tidal boundary layer. *Cont. Shelf Res.*, **2**, 109-126.
- Johns, W.E., 1988. Near-surface current measurements in the Gulf Stream

- using an upward-looking acoustic Doppler current profiler. *J. Atmos. Oceanic. Technol.*, **5**, 602-613.
- Kalkwijk, J.P.T., and R. Booij, 1986. Adaption of secondary flow in near-horizontal flow. *J. Hydraul. Res.*, **24**, 19-37.
- Lohrmann, A., B. Hackett, and L. P. Roed, 1990. High resolution measurements of turbulence, velocity and stress using a pulse-to-pulse coherent sonar. *J. Atmos. Oceanic. Technol.*, **7**, 19-37.
- Lueck, R.G., and Y. Lu, 1996. Observed logarithmic layer in a tidal channel.
- Schott, F., and W. Johns, 1987. Half-year-long measurements with a buoy-mounted acoustic Doppler current profile in the Somali Current. *J. Geophys. Res.*, **92**, 5169-5176.
- Soulsby, R. L., and K. R. Dyer, 1981. The form of the near-bed velocity profile in a tidally accelerating flow. *J. Geophys. Res.*, **86**, 8067-8074.
- Tang, C.L., and D.J. Belliveau, 1994. Vertical structure of currents on the northern Grand Bank –a view from a bottom mounted Acoustic Doppler Current Profiler. *Cont. Shelf Res.*, **12**, 1331-1347.
- Wolanski, E., J. Imberger, and M. L. Heron, 1984. Island wakes in shallow coastal waters. *J. Geophys. Res.*, **89**, 10553-10569.

van Haren, H., N. Oakey, and C. Garrett, 1994. Measurements of internal wave band eddy fluxes above a sloping bottom. *J. Mar. Res.*, **52**, 909-946.

## Figure captions

Figure 1. Area map and topography (depth in meters) of Cordova Channel and the location of ADCP. The positions of two deployments of the moored microstructure instrument (TAMI1 and TAMI2), a current meter (CMI), and the transmitter (T) and receiver (R) of a acoustic scintillation system deployed during the experiment are also shown.

Figure 2. The probing definition of ADCP.  $\theta (= 30^\circ)$  is the beam angle and  $\varphi_1, \varphi_2$  and  $\varphi_3$  are heading, pitch and roll angles.

Figure 3. One-day long vertical velocity at mid-depth, calculated for (roll angle)  $\varphi_3 = -2^\circ$  (thicker lines) and  $\varphi_3 = -3^\circ$  (thinner lines). The two upper curves are calculated from 20-minute smoothed beam velocities and the lower curves are 3-hour smoothed. The lower panel is a stick diagram of the horizontal flow at mid-depth.

Figure 4. Standard deviation of the 4-ping averaged, 1-m bin size of velocities along the four-beams, and its variation with the distance from the transducer. ADCP was mounted on a boat drifting in the almost slack water of the Saanich Inlet and the measurement was taken using the mode 4.

Figure 5. A sample of one-day of velocity data at mid-depth from the beam oriented in the downstream direction during ebb. The sampling time

interval is 3.05 s and each sample is the average of 4 pings. The 20-minute smoothed velocity and the residual high-frequency component are plotted. The stick diagram in the lower panel is the 20-minute mean horizontal velocity at that depth.

Figure 6. Time variation of the standard deviation along beams No.1 (thicker lines) and No.3 (thinner lines), at mid-depth (top panel) and 3.6 m above the sea bed (middle panel). The bottom panel is a stick diagram of the horizontal flow at mid-depth.

Figure 7. Time series of the high-pass velocity fluctuations along beams No.1 (top panel) and No.3 (bottom panel), at mid-depth (thinner lines) and 3.6 m above the seabed (thicker lines). This is a 20-minute section during the strong ebb starting at day 23.91.

Figure 8. Same with figure 7 but during the turning of flow starting at day 24.03.

Figure 9. Auto-correlation coefficients of the four high-pass beam velocity time series shown in figure 7.

Figure 10. Same as figure 9 but for the 20-minute data starting at day 24.6 during the weak flood.

Figure 11. The cross-channel (upper panel) and along-channel (lower panel)

velocity components measured at mid-depth (dots), and their harmonic fits including  $M_2$ ,  $S_2$ ,  $K_1$ ,  $O_1$  and a zero-frequency residue (solid curves). Differences between the measured flow and the harmonic fits are also shown by dots with an offset of  $-1.5 \text{ m s}^{-1}$ . The cross- and along-channel directions are pointing to  $75^\circ$   $345^\circ$  from the north respectively.

Figure 12. A polar coordinate diagram of 4.5 days of depth-averaged 20-minute mean velocity.

Figure 13. Upper panel: Direction of depth-mean velocity (thicker solid line) v. flow at 3.6 m above seabed (thinner solid line). Middle panels: Typical depth-variation in flow direction during flood (left) and ebb (right). Bottom panel: The change in shear direction with depth.

Figure 14. Polar coordinate diagrams of 4.5-day long flow (left) and shear (right) at  $Z = 3.6 \text{ m}$  height.

Figure 15. Color-coded depth-time sections of (a) streamwise and (b) transverse velocities; (c) 20-minute mean vertical flow; (d) streamwise flow shear with the log-layer height (dark curve); and (e) transverse velocity shear.

Figure 16. Time series of streamwise (upper panel) and transverse flow (lower panel) at the heights of 3.6 m (thicker solid lines), 15.6 m (thinner solid with dots) and 27.6 m (thinner solid).

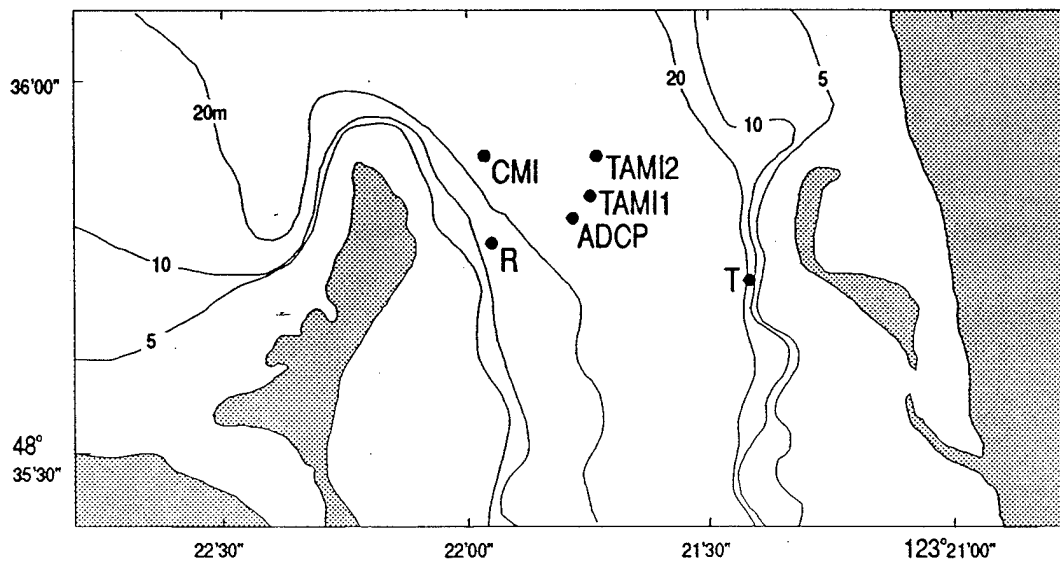
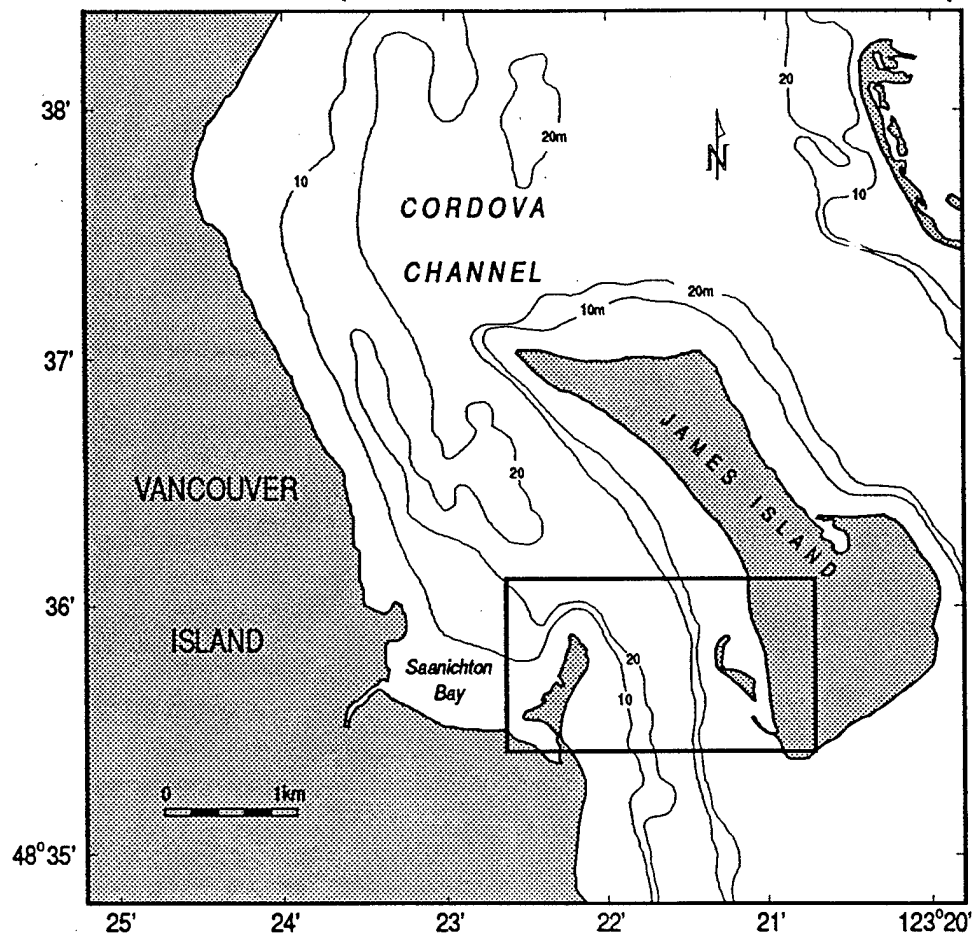


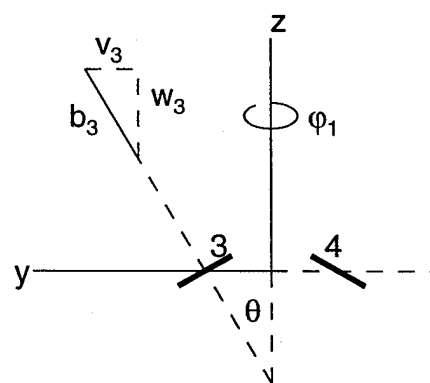
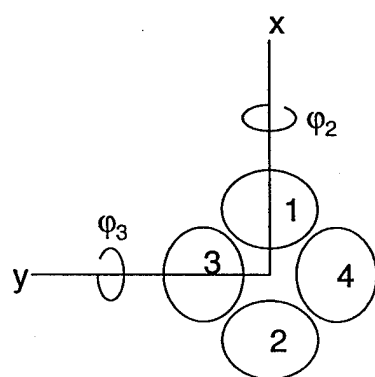
Figure 17. Profiles of streamwise (upper panel) and transverse flow (lower panel). The number of each profile indicates the index in the sequence of 20-minute segments starting from day 23.91.

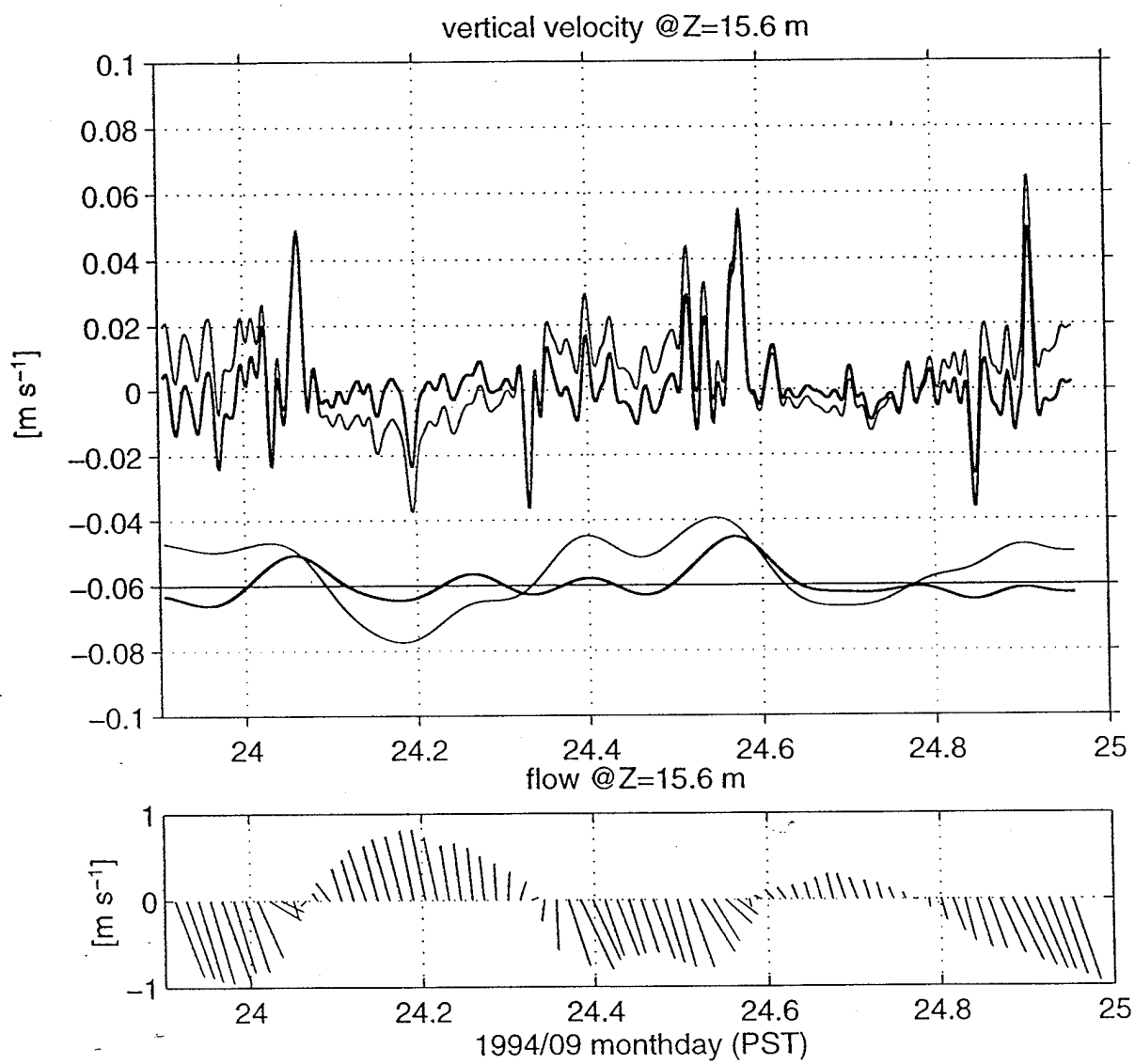
Figure 18. Same with figure 16 but for flow shear.

Figure 19. Same with figure 17 but for flow shear.

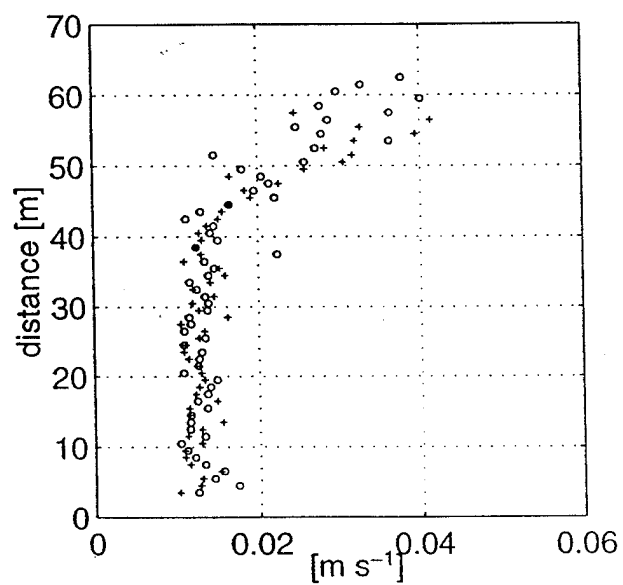
Figure 20. Upper panel: 20-minute mean vertical (thicker lines) and "error" velocities (thinner lines) at the heights of 15.6m, 3.6 m (offset by  $-0.05 \text{ m s}^{-1}$ ) and 27.6 m (offset by  $0.05 \text{ m s}^{-1}$ ). The sign of the "error" velocity is changed the same with the vertical velocity. Lower panel: Stick digram of 20-minute mean horizontal velocity.



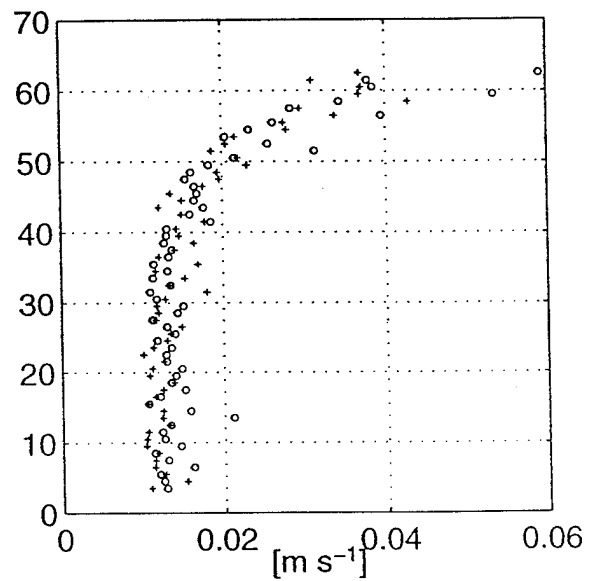




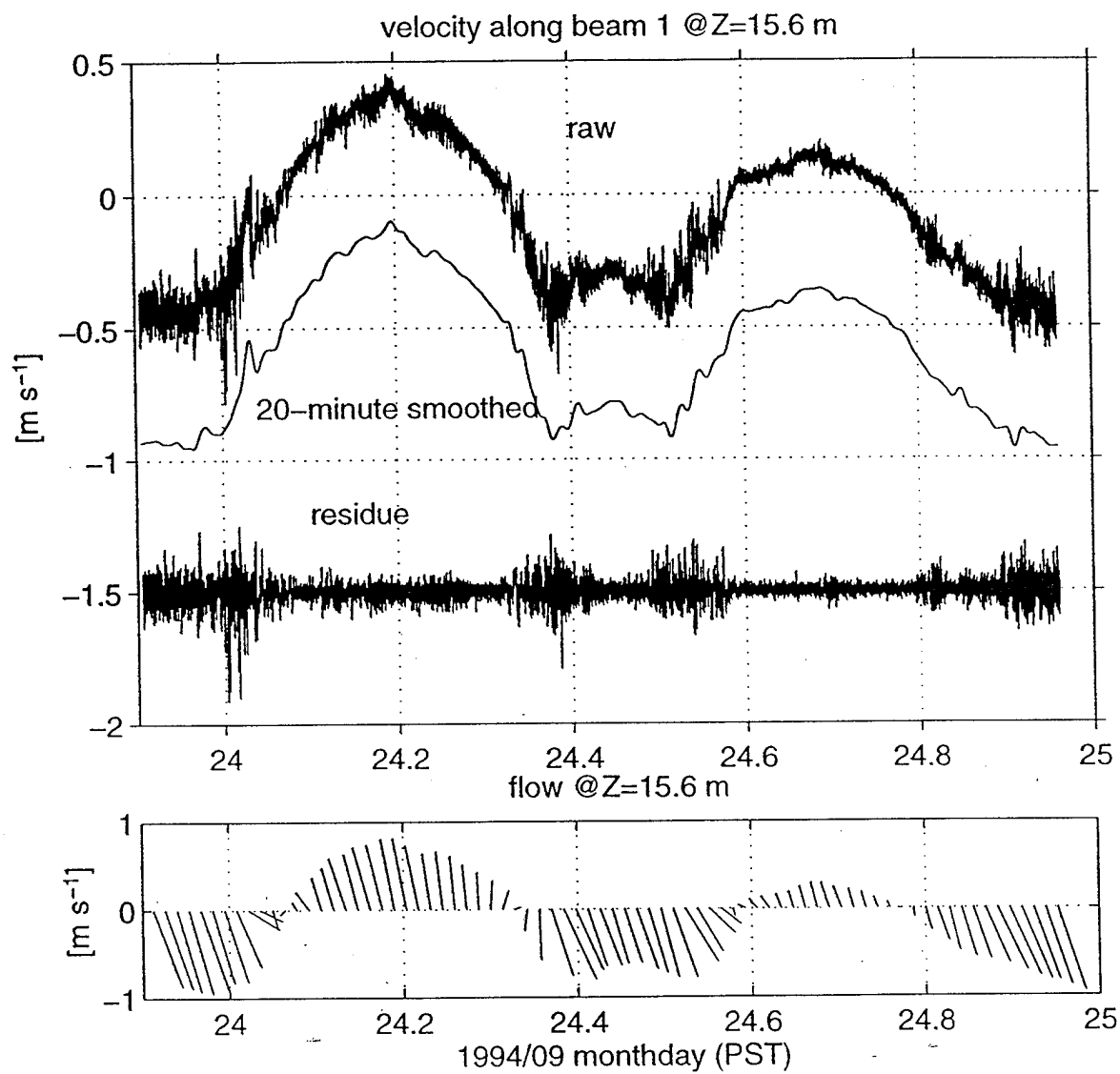
std: v1(o) v2(+)

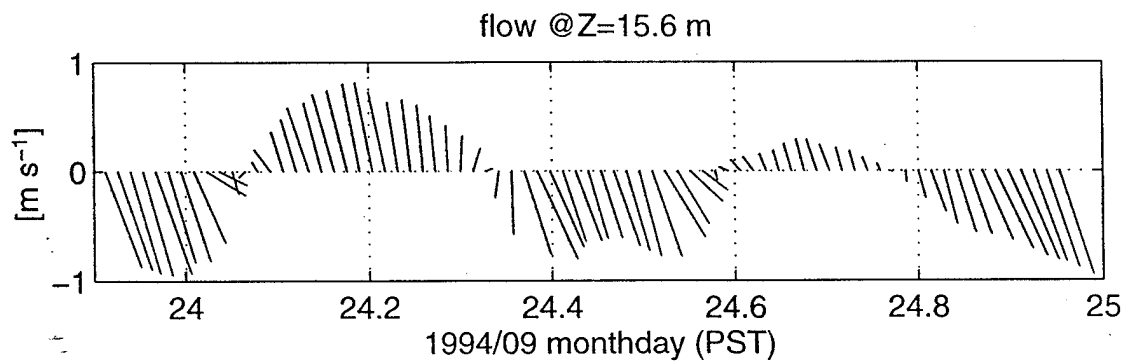
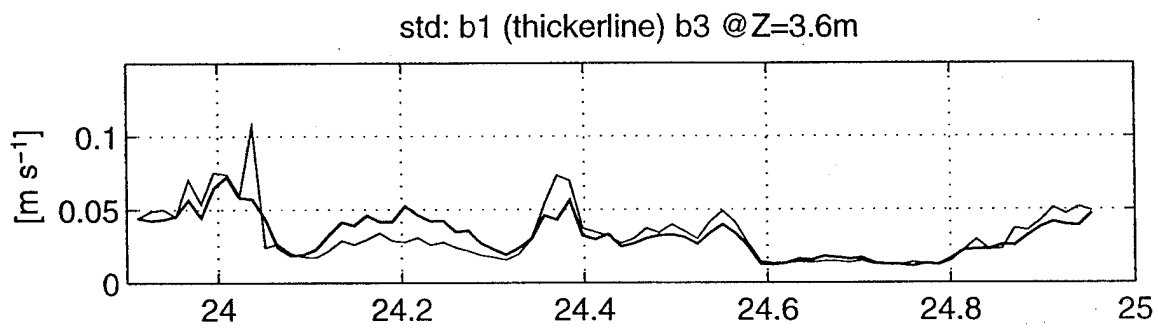
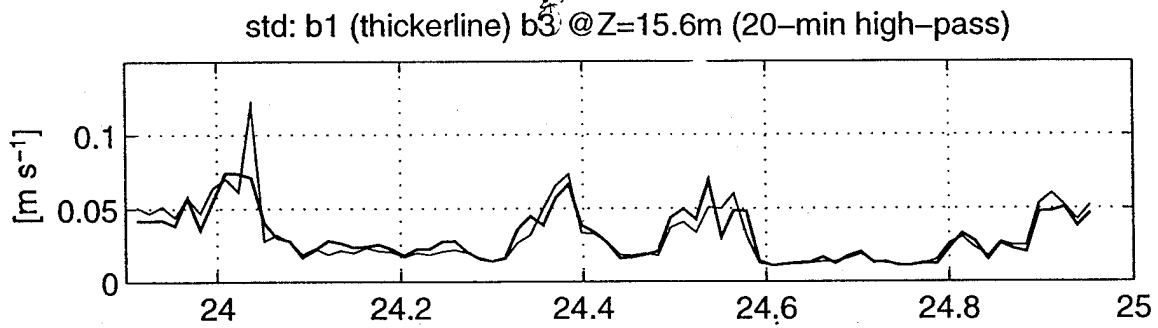


std: v3(o) v4(+)

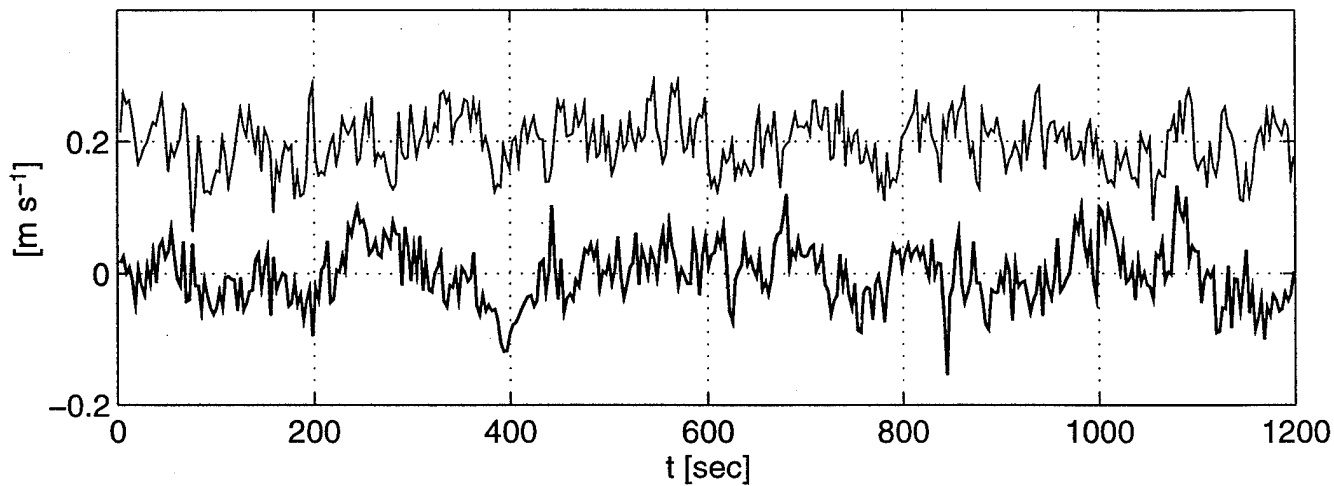


patbay6, cell size=1 m, 4 pings average

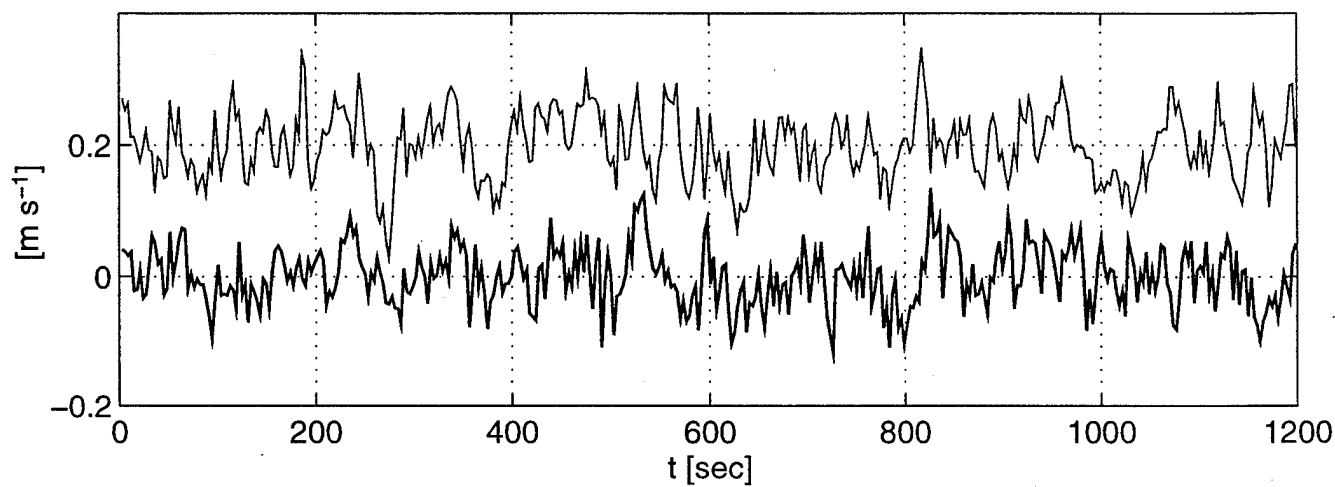




b1 @Z=3.6m (thicker line), 15.6m



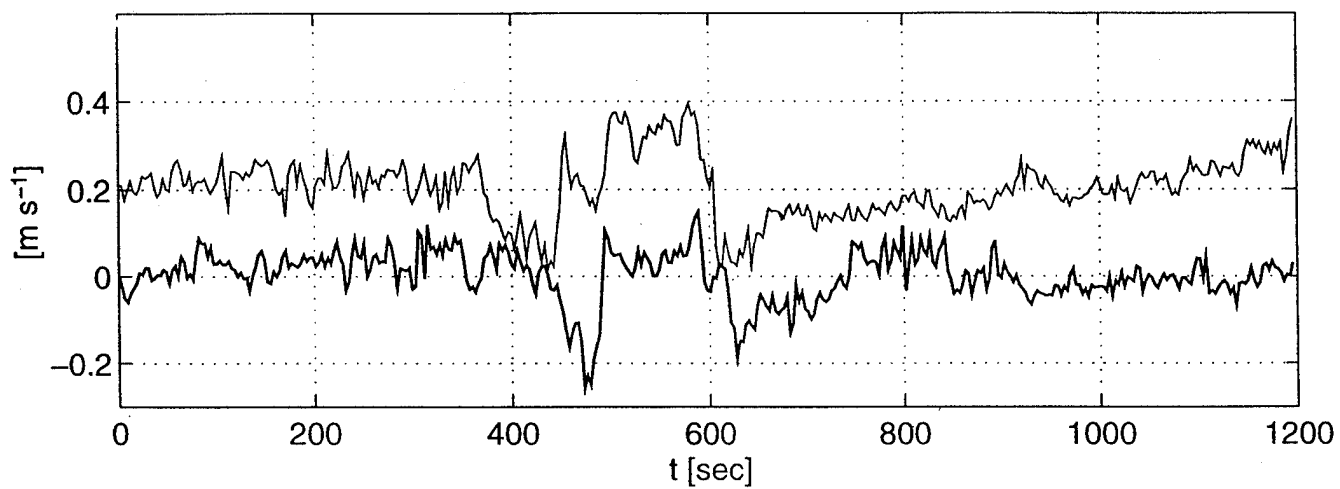
b3 @Z=3.6m (thicker line), 15.6m



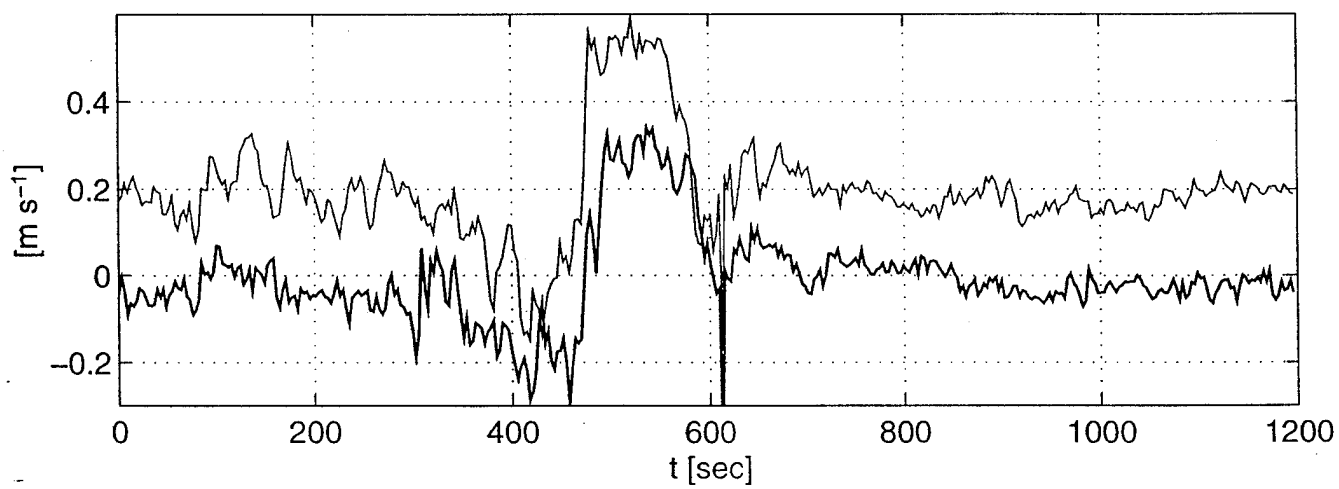
2 b6

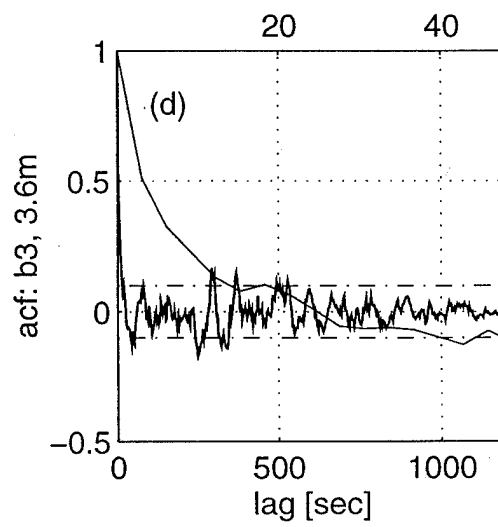
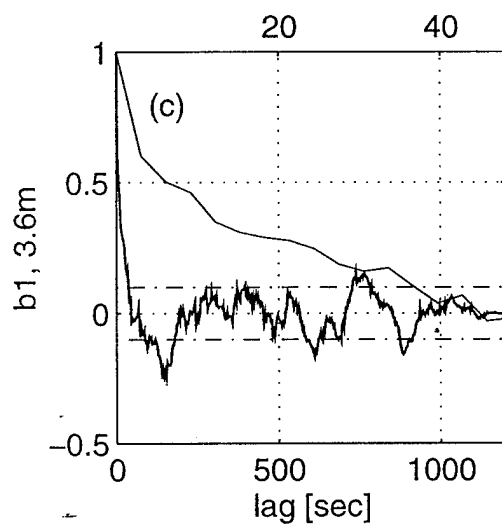
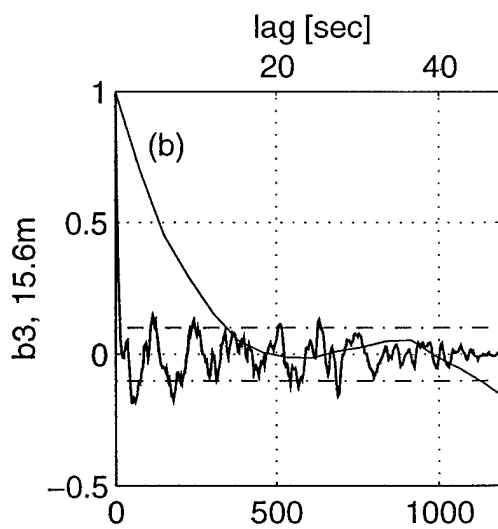
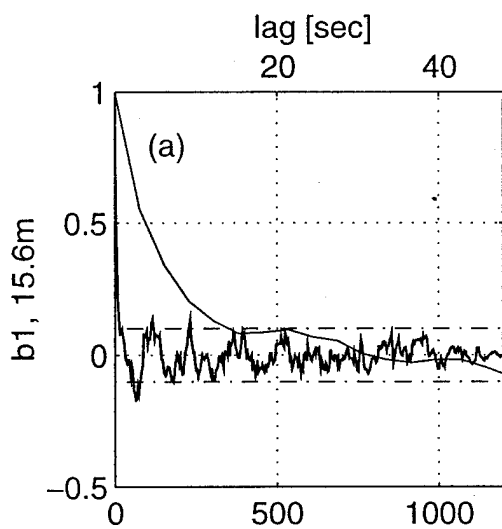


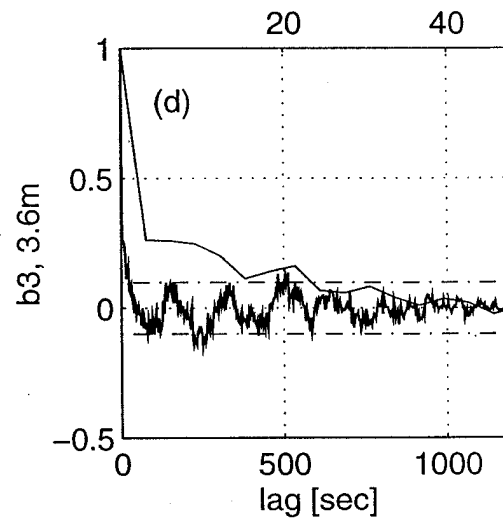
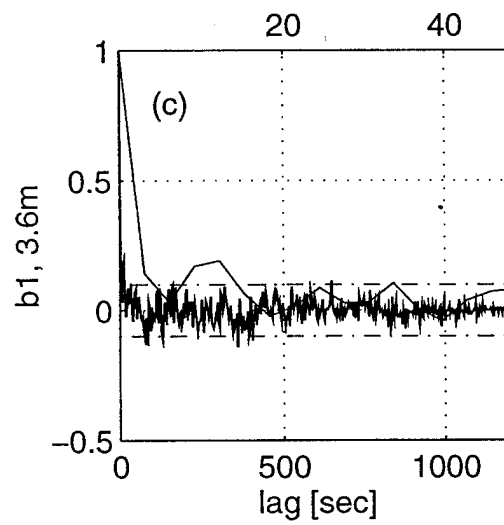
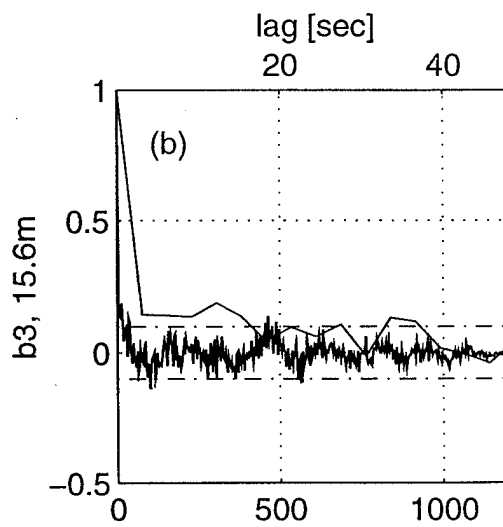
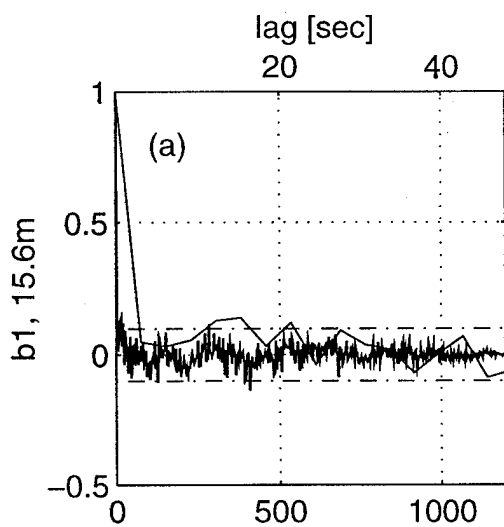
b1 @Z=3.6m (thicker line), 15.6m



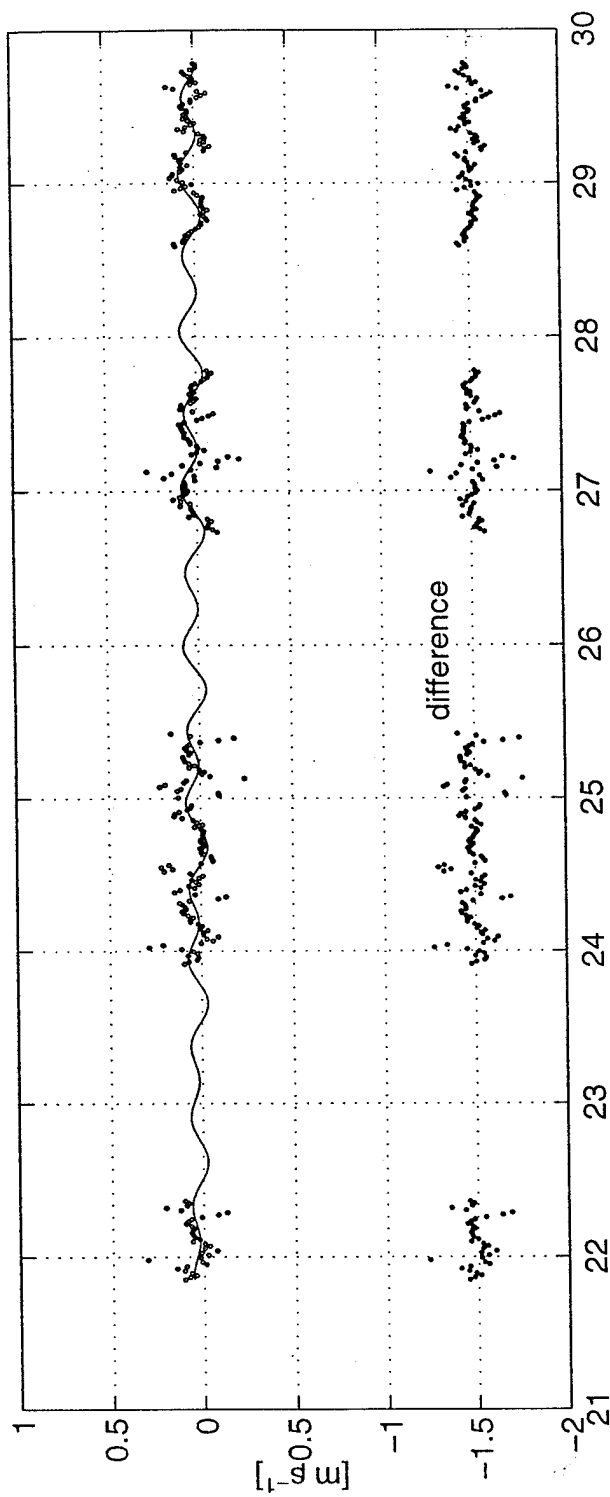
b3 @Z=3.6m (thicker line), 15.6m

*Handwritten signature*





Cross channel flow @ Z=15.6m fitted to  $M_2 S_2 K_1 O_1$



Along channel flow @ Z=15.6m fitted to  $M_2 S_2 K_1 O_1$

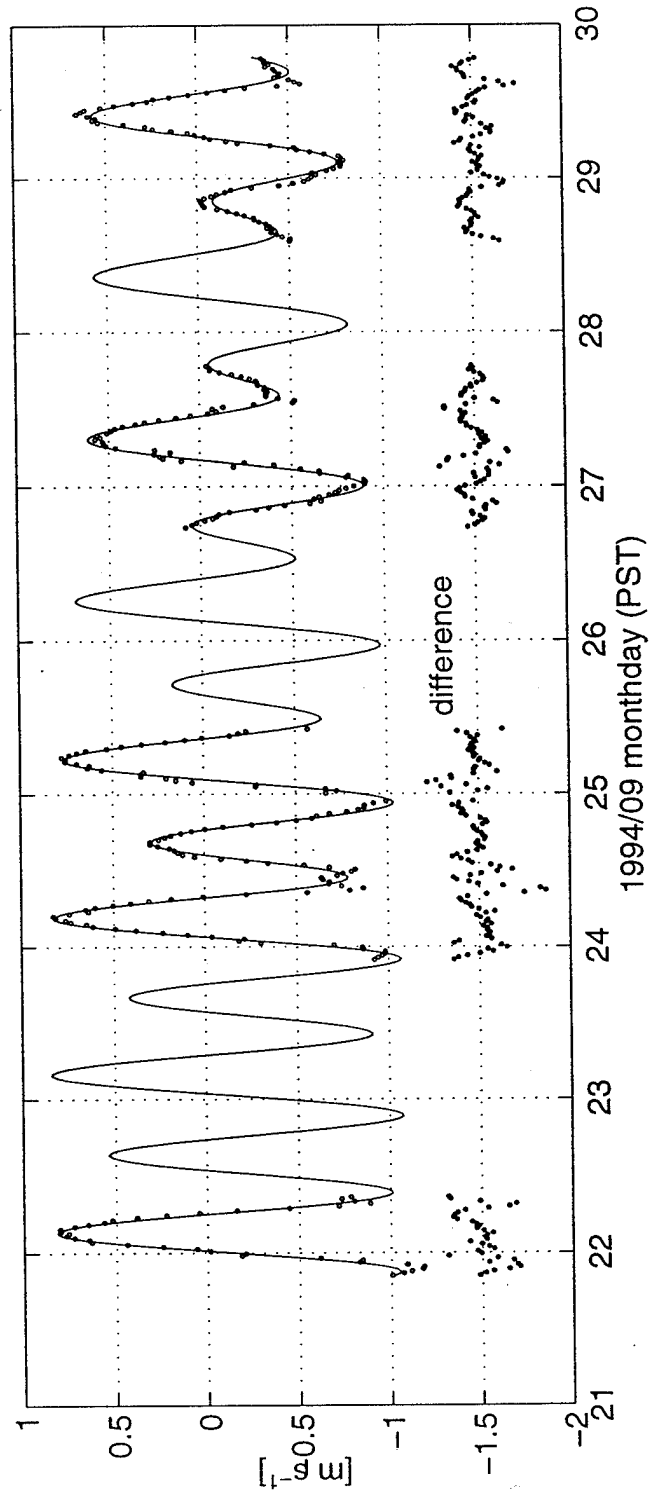
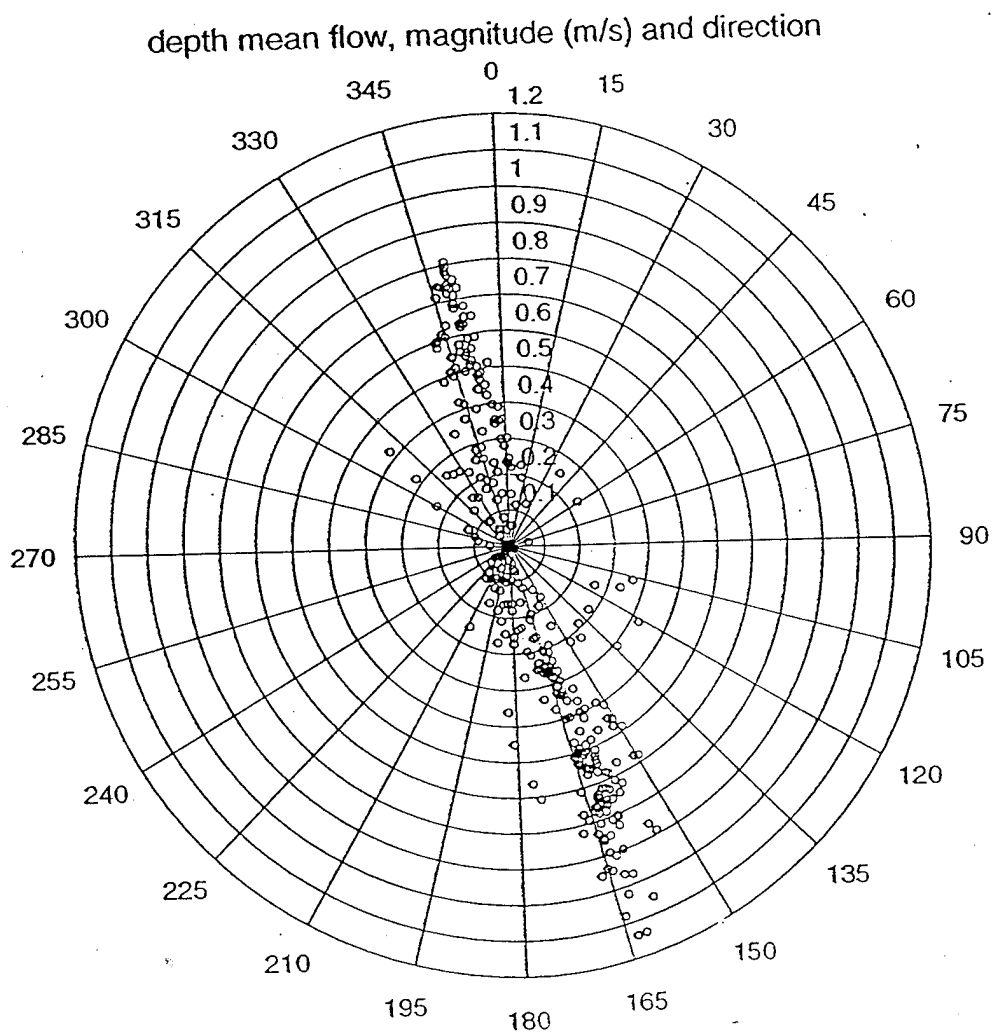


Fig. 12



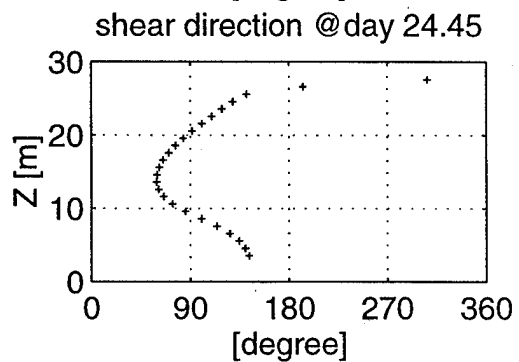
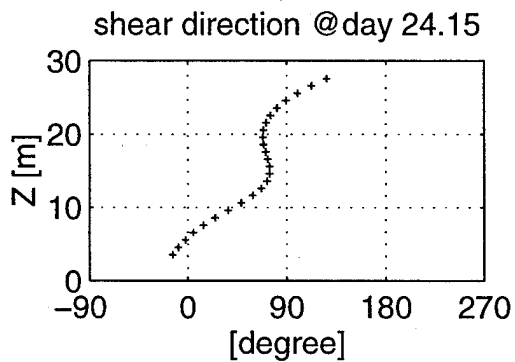
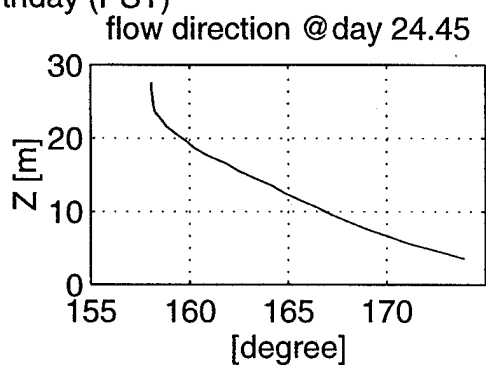
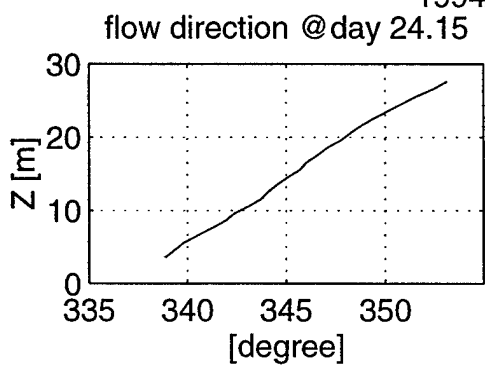
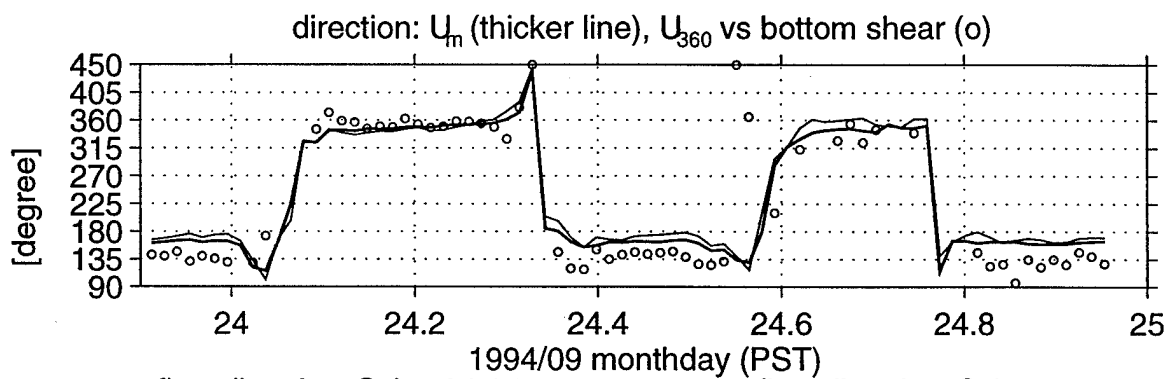
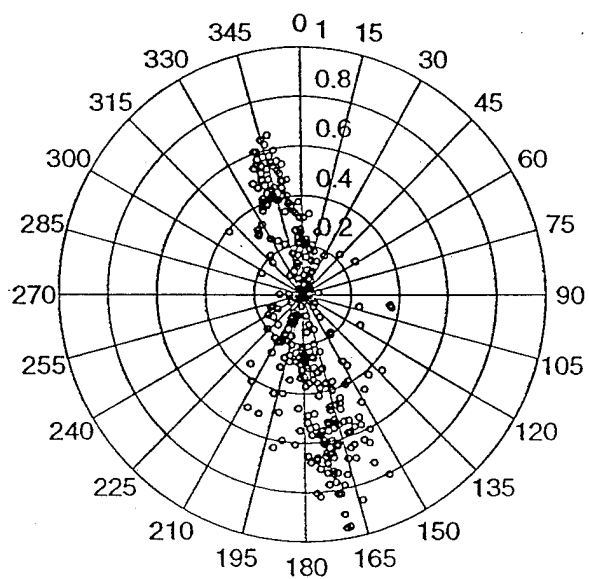
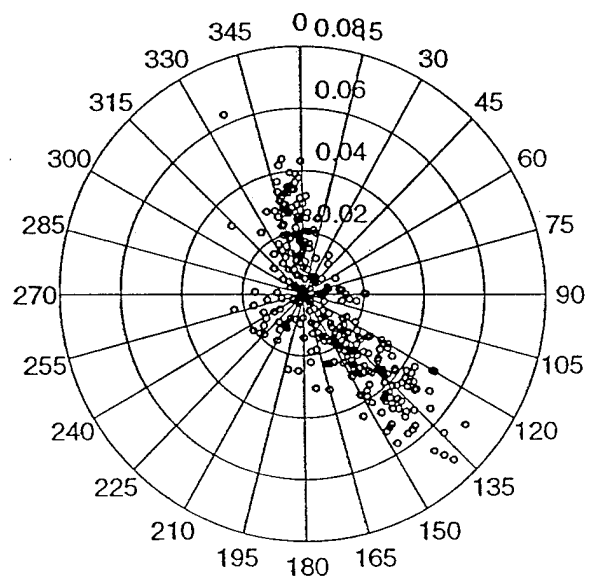


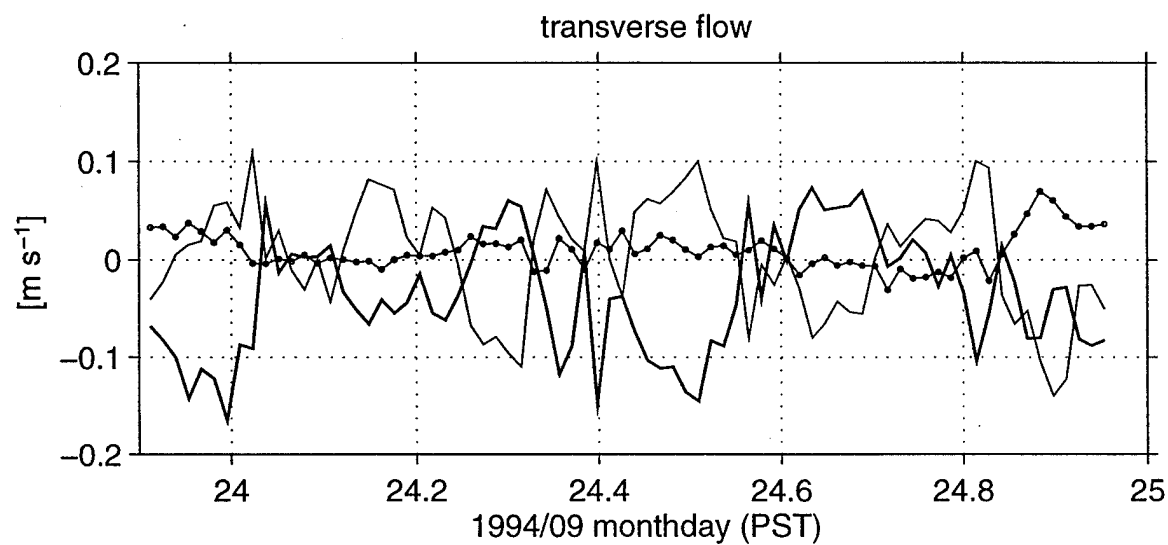
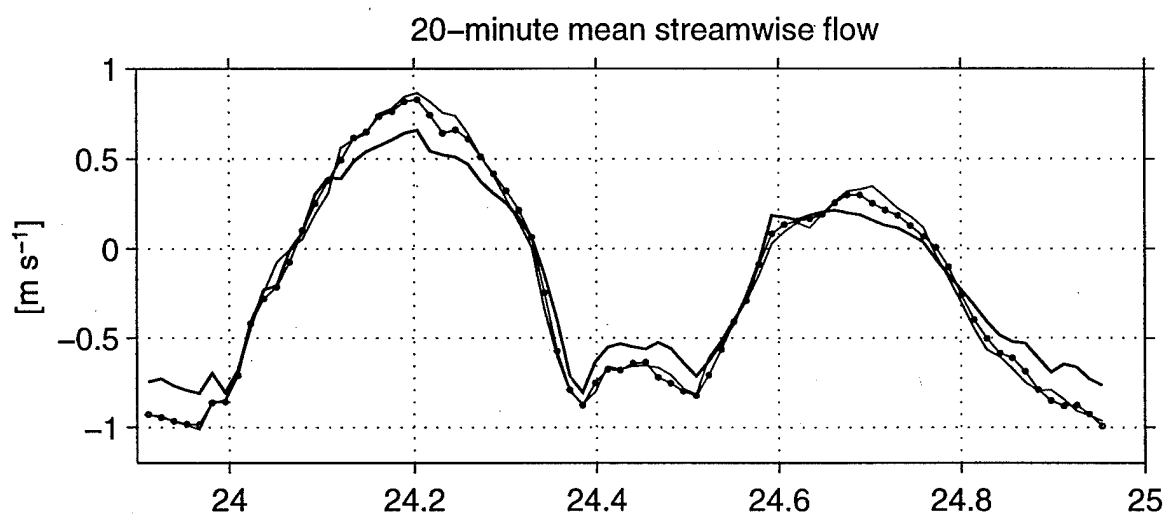
Fig. 14

flow @Z=3.6m



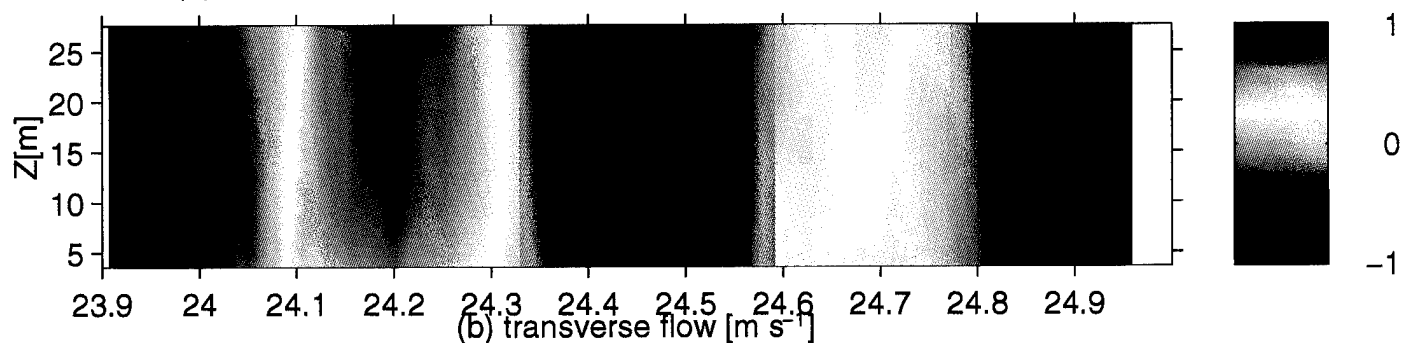
flow shear @Z=3.6m



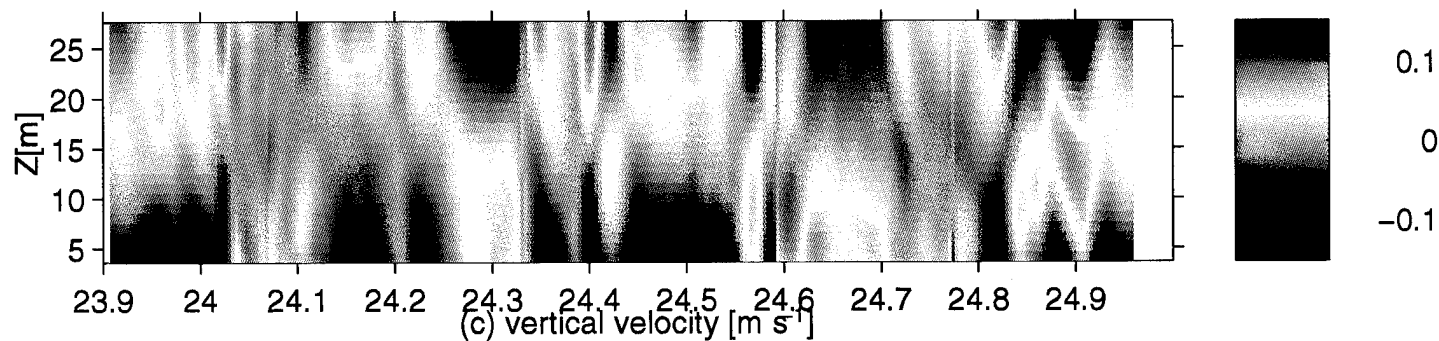




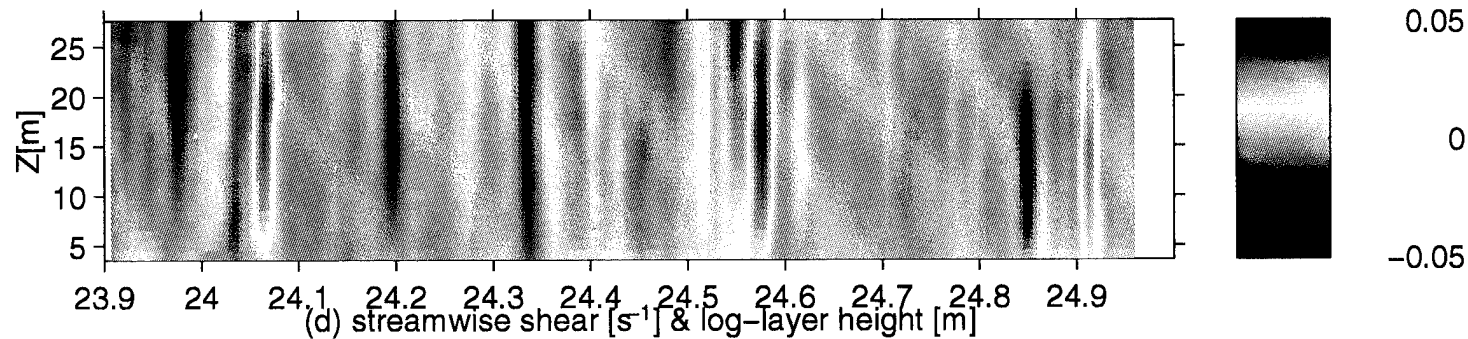
(a) Cordova Channel: 20-minute averaged streamwise flow [ $\text{m s}^{-1}$ ]



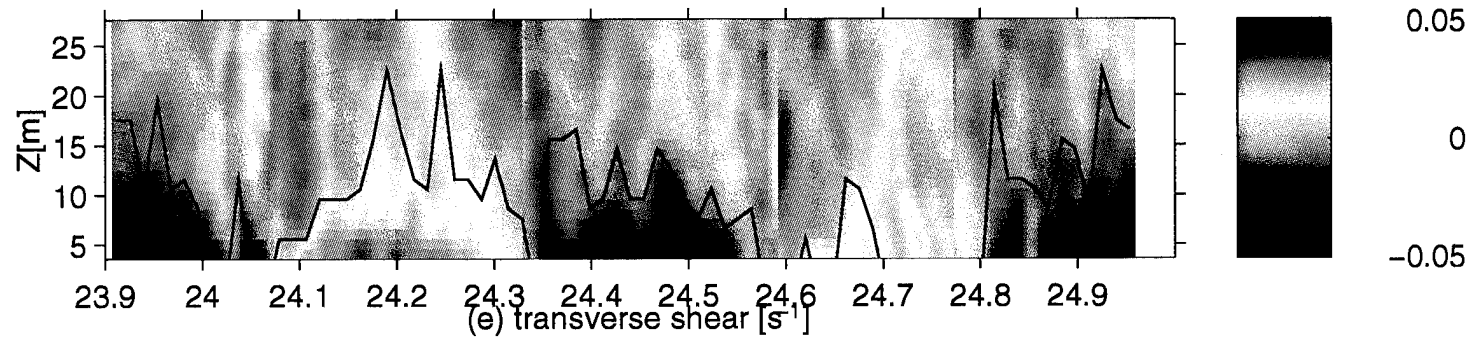
(b) transverse flow [ $\text{m s}^{-1}$ ]



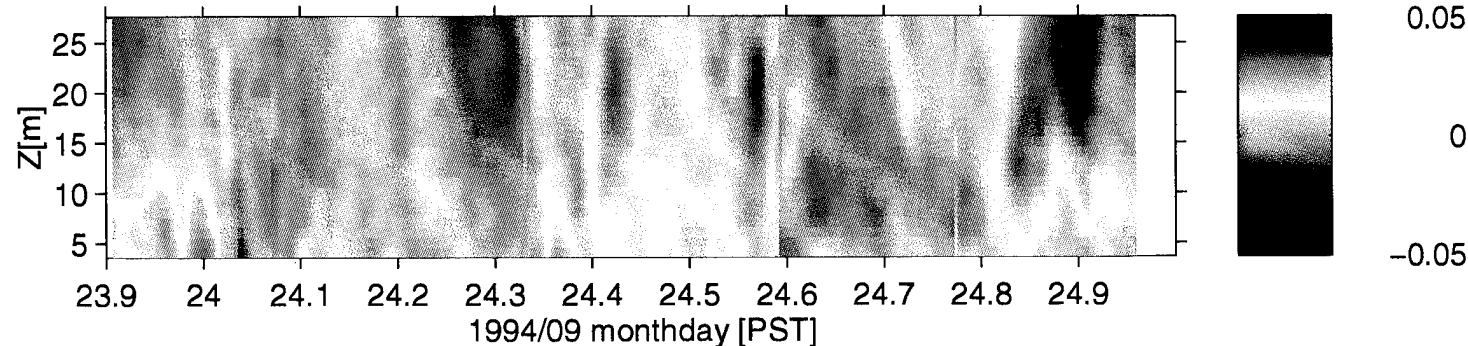
(c) vertical velocity [ $\text{m s}^{-1}$ ]



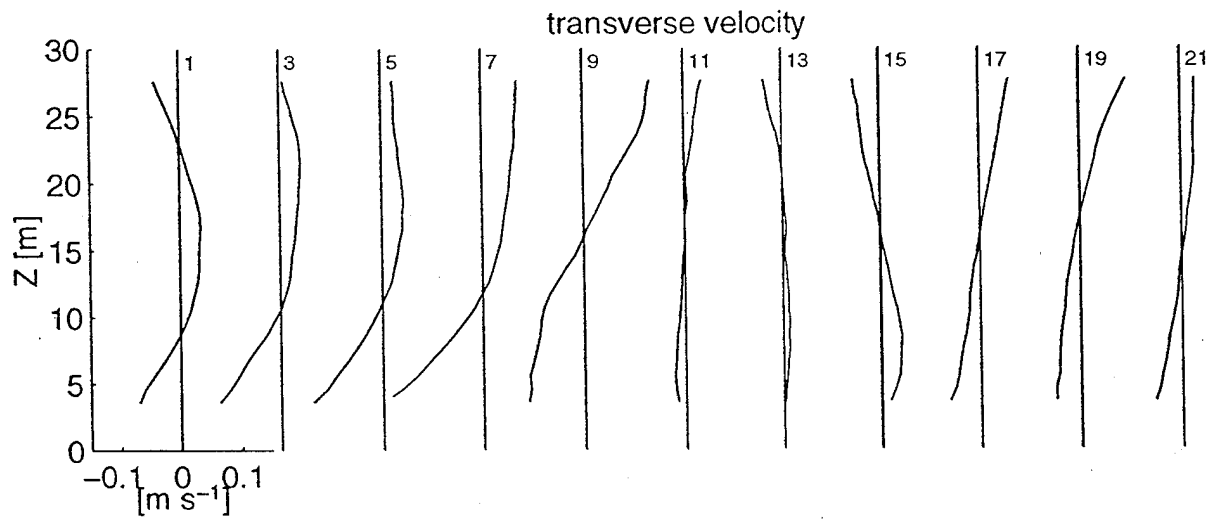
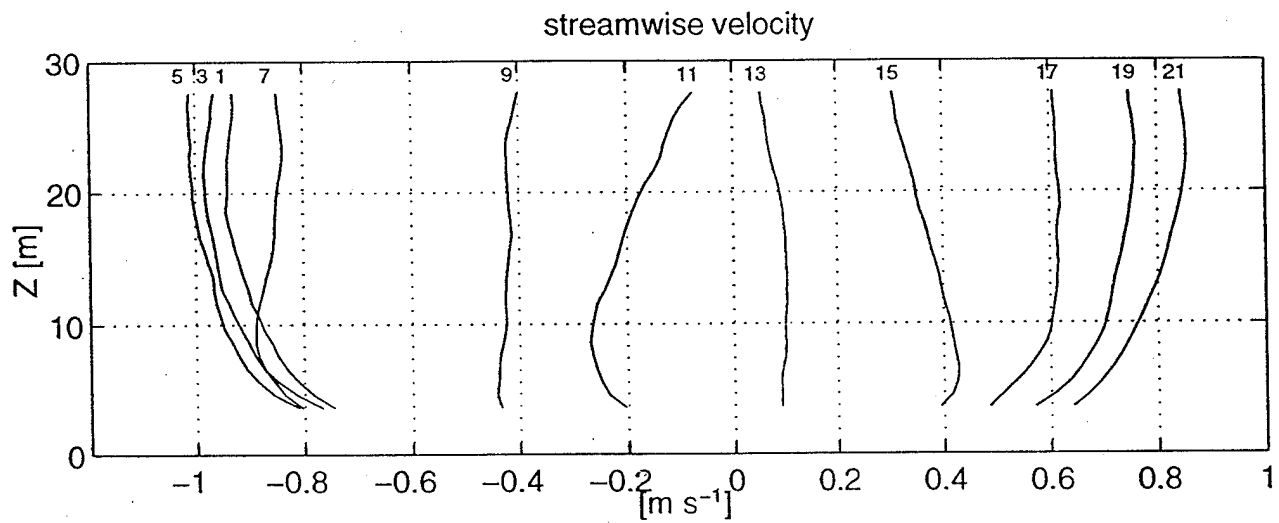
(d) streamwise shear [ $\text{s}^{-1}$ ] & log-layer height [m]

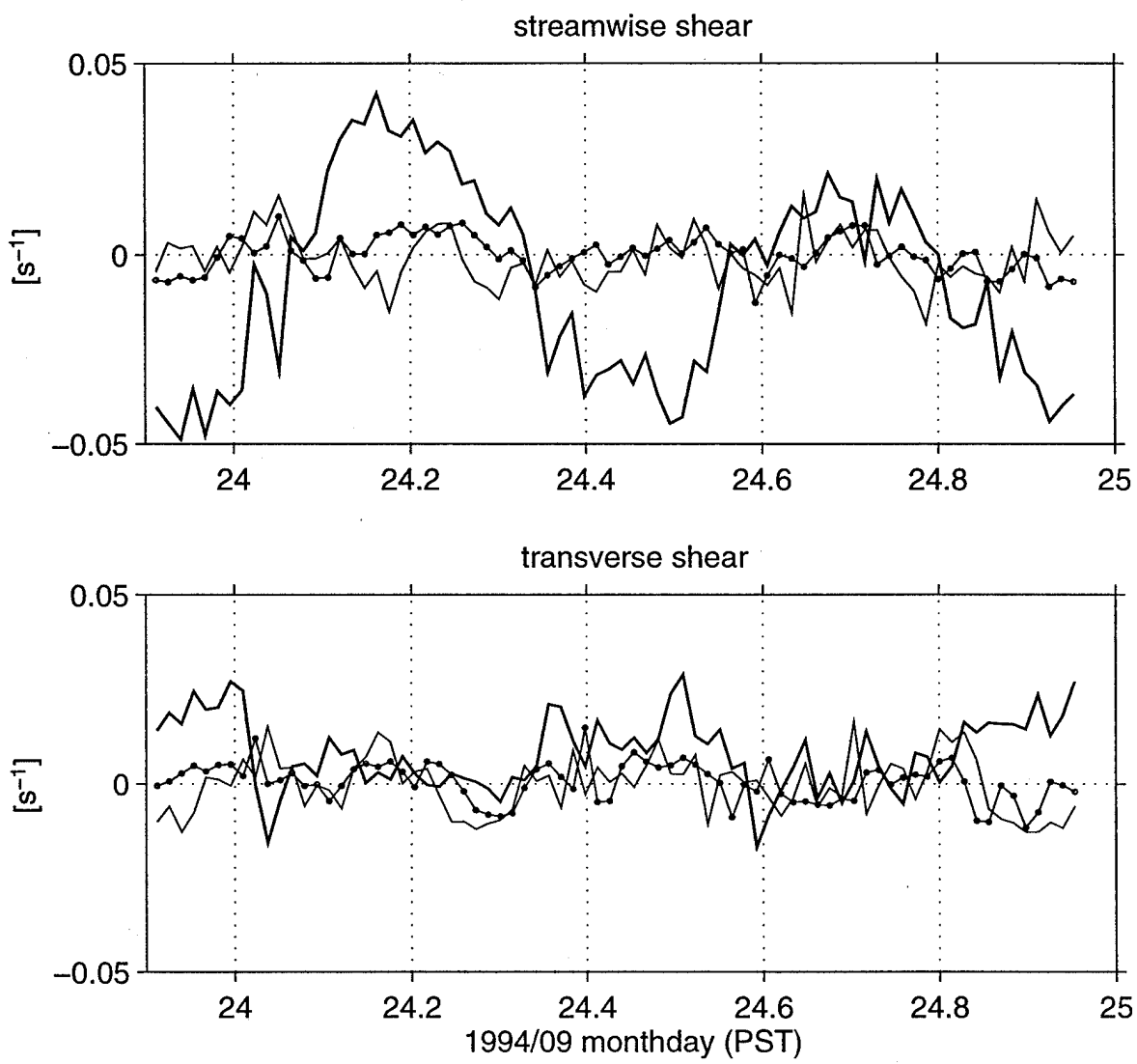


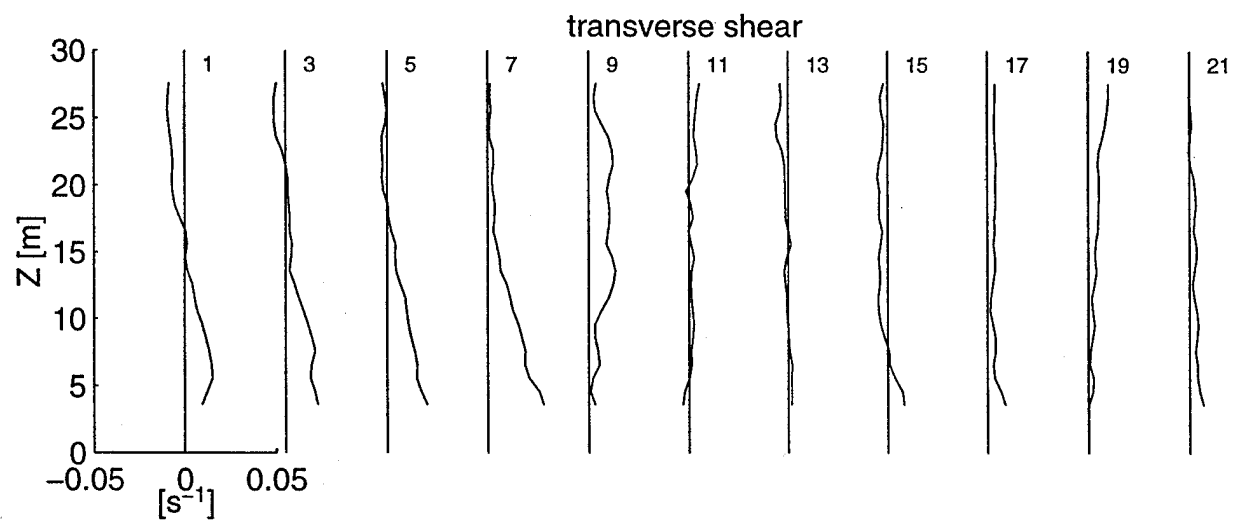
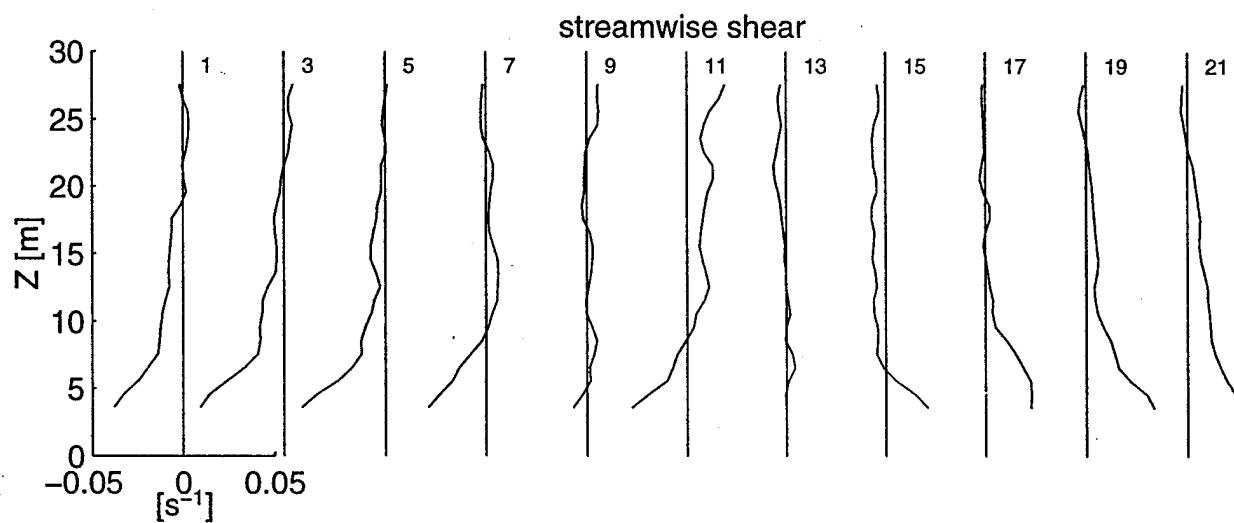
(e) transverse shear [ $\text{s}^{-1}$ ]

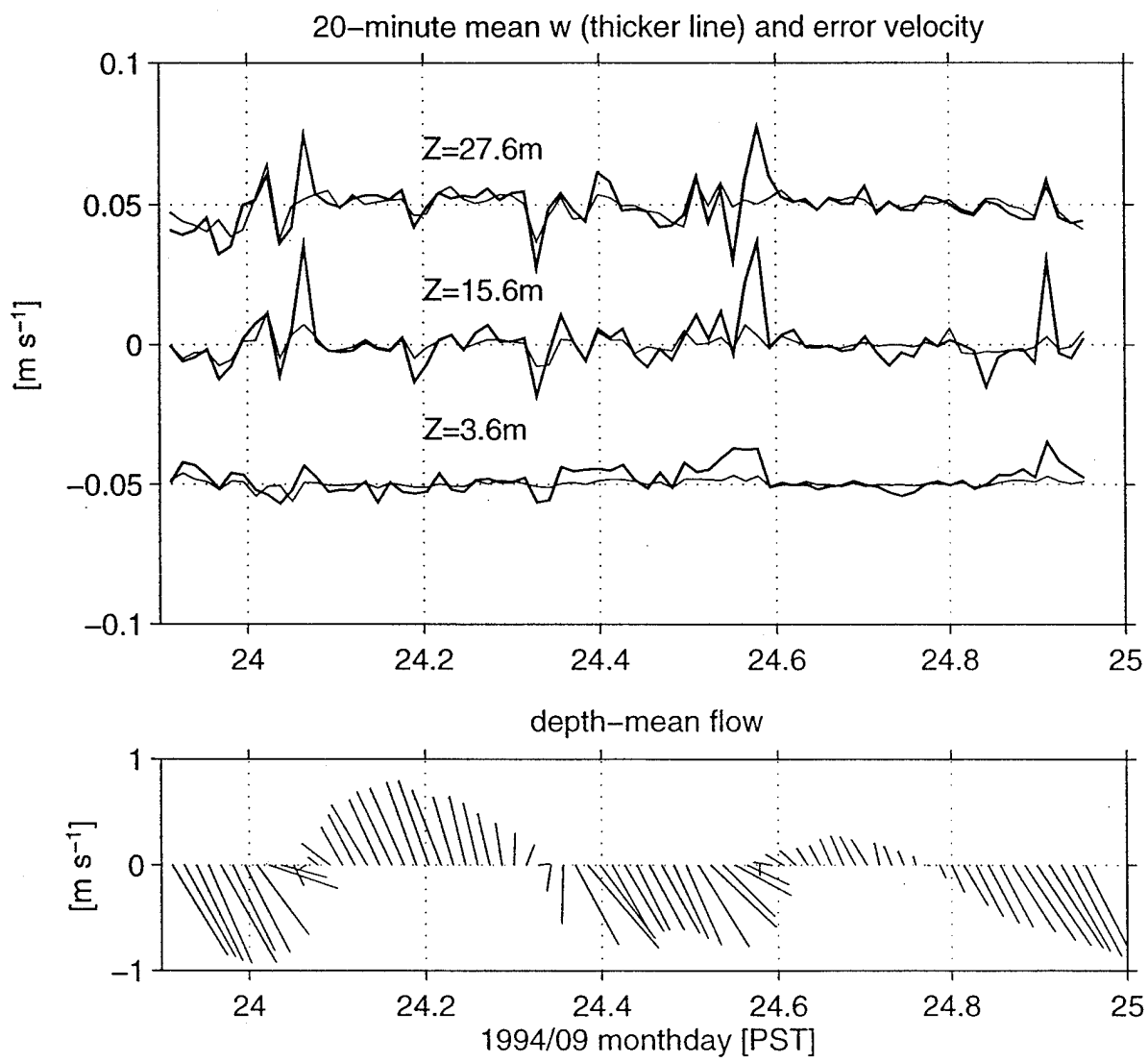


17  
Fig. ~~17~~ 9









REPORT DOCUMENTATION PAGE			Form Approved OMB No. 0704-0188	
Public reporting burden for this collection of information is estimated to average 1 hour per response, including the time for reviewing instructions, searching existing data sources, gathering and maintaining the data needed, and completing and reviewing the collection of information. Send comments regarding this burden estimate or any other aspect of this collection of information, including suggestions for reducing this burden, to Washington Headquarters Services, Directorate for Information Operations and Reports, 1215 Jefferson Davis Highway, Suite 1204, Arlington, VA 22202-4302, and to the Office of Management and Budget, Paperwork Reduction Project (0704-0188), Washington, DC 20503.				
1. AGENCY USE ONLY (Leave blank)		2. REPORT DATE 15 March 1996	3. REPORT TYPE AND DATES COVERED Final: 01 March 1993 - 29 Feb 1996	
4. TITLE AND SUBTITLE  Flow Measurements in a Tidal Channel using an Acoustic Doppler Current Profiler			5. FUNDING NUMBERS  G-N00014-93-1-0362	
6. AUTHOR(S)  Rolf Lueck				
7. PERFORMING ORGANIZATION NAME(S) AND ADDRESS(ES) Centre for Earth and Ocean Research University of Victoria P.O. Box 1700 Victoria, B.C., V8W 2Y2, Canada			8. PERFORMING ORGANIZATION REPORT NUMBER CEOR Report: 96-2	
9. SPONSORING/MONITORING AGENCY NAME(S) AND ADDRESS(ES) Department of the Navy Office of Chief of Naval Research 800 Quincy Street, Code 1512 AW Arlington, Virginia, 22217-5000			10. SPONSORING/MONITORING AGENCY REPORT NUMBER	
11. SUPPLEMENTARY NOTES  To be published in Continental Shelf Research				
12a. DISTRIBUTION / AVAILABILITY STATEMENT  Unlimited Availability			12b. DISTRIBUTION CODE	
13. ABSTRACT (Maximum 200 words)  An acoustic Doppler current profiler (ADCP) was applied to measure the three-dimensional flow field in a tidal channel along the coast of Vancouver Island, British Columbia. The ADCP was rigidly mounted to the bottom in the center of the channel, and rapidly sampled the velocity profiles along its inclined beams. The data were directly read by a computer on shore. This method of deployment allows for an explicit estimate of the uncertainty of mean velocity due to turbulence, and obtains the weak signal of vertical velocity. The mean flow vector is derived from the measured beam velocities under the assumption that the flow is statistically homogeneous in the horizontal plane over the distance separating the inclined beams of the ADCP.  The depth-time variations of velocity and shear in this natural channel are more complex than is found in idealized one-dimensional channel flow, which seldom occurs in nature. The channel contains strong secondary circulation, intense up- and down-welling intervals, frequent shear reversals and a substantial amount of transverse velocity shear.				
14. SUBJECT TERMS  Tidal Currents, Acoustic Doppler Profiler, Shear			15. NUMBER OF PAGES 60	
16. PRICE CODE			17. SECURITY CLASSIFICATION OF ABSTRACT UNCLASSIFIED	
18. SECURITY CLASSIFICATION OF THIS PAGE UNCLASSIFIED		19. SECURITY CLASSIFICATION OF ABSTRACT UNCLASSIFIED		20. LIMITATION OF ABSTRACT

## GENERAL INSTRUCTIONS FOR COMPLETING SF 298

The Report Documentation Page (RDP) is used in announcing and cataloging reports. It is important that this information be consistent with the rest of the report, particularly the cover and title page. Instructions for filling in each block of the form follow. It is important to *stay within the lines* to meet optical scanning requirements.

### Block 1. Agency Use Only (Leave blank).

**Block 2. Report Date.** Full publication date including day, month, and year, if available (e.g. 1 Jan 88). Must cite at least the year.

**Block 3. Type of Report and Dates Covered.** State whether report is interim, final, etc. If applicable, enter inclusive report dates (e.g. 10 Jun 87 - 30 Jun 88).

**Block 4. Title and Subtitle.** A title is taken from the part of the report that provides the most meaningful and complete information. When a report is prepared in more than one volume, repeat the primary title, add volume number, and include subtitle for the specific volume. On classified documents enter the title classification in parentheses.

**Block 5. Funding Numbers.** To include contract and grant numbers; may include program element number(s), project number(s), task number(s), and work unit number(s). Use the following labels:

C - Contract	PR - Project
G - Grant	TA - Task
PE - Program Element	WU - Work Unit Accession No.

**Block 6. Author(s).** Name(s) of person(s) responsible for writing the report, performing the research, or created with the content of the report. If editor or compiler, this should follow the name(s).

**Block 7. Performing Organization Name(s) and Address(es).** Self-explanatory.

**Block 8. Performing Organization Report Number.** Enter unique alphanumeric report number assigned by the organization performing the report.

**Block 9. Sponsoring Agency Name(s) and Address(es).** Self-explanatory.

U.S. GOVERNMENT PRINTING OFFICE: 1980

**Block 12a. Distribution/Availability Statement.** Denotes public availability or limitations. Cite any availability to the public. Enter additional limitations or special markings in all capitals (e.g. NOFORN, REL, ITAR).

**DOD** - See DoDD 5230.24, "Distribution Statements on Technical Documents."

**DOE** - See authorities.

**NASA** - See Handbook NHB 2200.2.

**NTIS** - Leave blank.

### Block 12b. Distribution Code.

**DOD** - Leave blank.

**DOE** - Enter DOE distribution categories from the Standard Distribution for Unclassified Scientific and Technical Reports.

**NASA** - Leave blank.

**NTIS** - Leave blank.

**Block 13. Abstract.** Include a brief (*Maximum 200 words*) factual summary of the most significant information contained in the report.

**Block 14. Subject Terms.** Keywords or phrases identifying major subjects in the report.

**Block 15. Number of Pages.** Enter the total number of pages.

**Block 16. Price Code.** Enter appropriate price code (*NTIS only*).

**Blocks 17. - 19. Security Classifications.** Self-explanatory. Enter U.S. Security Classification in accordance with U.S. Security Regulations (i.e., UNCLASSIFIED). If form contains classified information, stamp classification on the top and bottom of the page.

**Block 20. Unavailability Statement.** If the report is unavailable, enter the reason for unavailability. If the report is available, enter the source of the report. If the report is available, enter the source of the report. If the report is available, enter the source of the report.